Delft University of Technology
Master of Science Thesis in Computer and Embedded Systems Engineering

Decimeter-Level Localization Using Single-Anchor Multipath UWB Signals

Saransh Goel

TU Delft Delft University of Technology

Decimeter-Level Localization Using Single-Anchor Multipath UWB Signals

Master of Science Thesis in Computer and Embedded Systems Engineering

Embedded Systems Group
Faculty of Electrical Engineering, Mathematics and Computer Science
Delft University of Technology
Van Mourik Broekmanweg 6, 2628 XE Delft, The Netherlands

Saransh Goel

29th May 2024

Author
Saransh Goel
Title
Decimeter-Level Localization Using Single-Anchor Multipath UWB Signals
MSc Presentation Date
29th May 2024

Graduation Committee

Qing Wang	Delft University of Technology
Marco Zuniga	Delft University of Technology
Guido Dolmans	IMEC, The Netherlands

Abstract

This research investigates the impact of multipath signals in UWB communications and explores their potential to improve localization accuracy of tags using the additional information captured in the Channel Impulse Response (CIR). While traditional localization typically relies on multiple anchors, this study focuses on using a single anchor and creating multiple Virtual Anchors (VAs) through MultiPath Components (MPCs). The research proposes algorithms such as likelihood, algebraic, and fminsearch methods, and tests their performance through simulations in environments with anchors, tags, and reflective surfaces.

After confirming the feasibility of using reflection multipath signals for localization through the simulations, experiments were conducted with NXP's SR150 UWB tags, which collect CIR data via two antennas. An indoor environment was set up with two MPCs and a strategically placed anchor. Data was collected from various tag locations and analyzed using the different localization methods.

The collected CIR data revealed additional reflections, notably from the ceiling and ground, which sometimes interfered with the desired MPC reflections. To address this, data cleaning techniques were implemented for the likelihood method, and the two antennas were used to approximate the AoA in the fminsearch and multilateration methods.

The final results demonstrated that the likelihood method achieved an average localization error of 26 cm, the fminsearch method 20.7 cm, and the algebraic method 24 cm. While the fminsearch method provided the best accuracy, it required data from two antennas, unlike the likelihood method, which only needed one. The fminsearch method showed improved accuracy near MPCs, though its performance declined as the tag moved further away. This suggests its potential for applications where AoA is large, as traditional methods become less accurate beyond 60-degree angles.

"Every signal has a spectrum and the spectrum determines the the signal" –
Professor Brad Osgood, Stanford University

Preface

I present to you my Master's Thesis on "Decimeter-Level Localization Using Single-Anchor Multipath UWB Signals." Over the past two years, my master's journey has been an immensely rewarding experience, filled with significant learning and personal growth. The thesis journey, spanning ten months, has provided me with profound insights into the realm of academia.

I extend my heartfelt gratitude to my supervisor at IMEC, Dr. Guido Dolmans, for introducing me to this topic and for his unwavering support and guidance throughout the project. I am equally grateful to Dr. Qing Wang for supervising and guiding me through my thesis journey. Additionally, I would like to thank Dr. Marco Zuniga for agreeing to join my thesis committee.

I am also thankful to my friends at TU Delft, who provided constant support and guidance and were like a family away from home. Lastly, I would like to express my deepest appreciation to my parents for making it possible for me to pursue such an exceptional education and for helping me become a better person. Their support and encouragement have been invaluable.

Saransh Goel

Delft, The Netherlands
29th May 2024

Contents

Chapter 1

Introduction

This chapter introduces the basics of Ultra Wide Band (UWB) localization and emphasizes its prospective significance in our daily lives. We all have encountered situations where searching for lost items like keys or mobile phones consumed hours of our time. UWB localization offers a solution to mitigate these challenges, particularly in indoor settings where conventional technologies such as GPS satellites struggle to penetrate through metal or concrete structures.

1.1 What is an Ultra Wide Band signal?

Ultra-Wideband (UWB) signal is a type of radio signal that utilizes a very large bandwidth, typically spanning several GHz of the electromagnetic spectrum. UWB signals are characterized by their short duration, high data rates, and low power spectral density. They have a relatively low power level and a very wide frequency range, which sets them apart from traditional narrowband and spread-spectrum signals. There are several applications that utilize UWB signals. Recently, UWB has been widely adopted for localization purposes in mobile phones. Many modern mobile phones are equipped with UWB chips, enabling them to communicate with other UWB devices.

UWB is also being utilized in modern cars for secure locking and unlocking. By using Scrambled Timestamp Sequence (STS), UWB makes passive keyless entry resilient to relay attacks, enhancing vehicle security. UWB is gradually being integrated into more applications due to its ability to provide indoor localization with centimeter-level accuracy.

1.2 Extractable Information from UWB Signals

From UWB signals, various types of information can typically be extracted, including distance and angle. Below is an outline of the information that can be obtained.

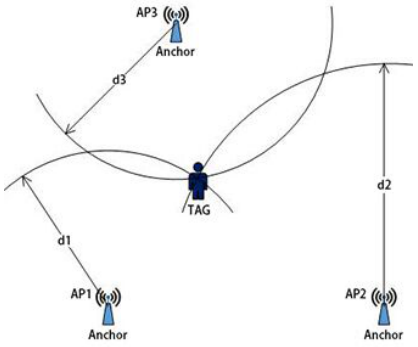

Figure 1.1: **Time Difference of Arrival (adapted from [42]).**

1.2.1 Distance

UWB signals are capable of transmitting extremely short pulses, which makes it possible to measure the time it takes for a signal to travel from a transmitter (UWB anchor) to a receiver (UWB tag) and back. By precisely measuring this time, one can calculate the distance between the anchor and the tag using the speed of light (denoted as c), known as Time-of-Flight measurement (ToF) [46]:

$$Distance = ToF * c. \tag{1.1}$$

Using Equation (1.1) we can calculate the distance between two UWB devices.

Time Difference of Arrival (TDoA) is a technique employed in UWB positioning systems to ascertain the whereabouts of a wireless device, typically within a limited geographical area. The estimation of the tag's location using TDoA primarily relies on multiple anchor points. When the tag emits a signal, all the anchors receive it and record a timestamp at the moment of signal reception. These timestamps are subsequently used to calculate the distances between the anchors and the tag, as described by Equation (1.1). With these distances in hand, the tag's location can be determined through a triangulation process as shown in Figure 1.1.

1.2.2 Angle

UWB can also be used to determine the direction from which a signal arrives at a receiver. When multiple antennas are interconnected to form an antenna array situated on an anchor, it becomes viable to utilize the Phase Difference of Arrival (PDoA) between these antennas to determine an angle, as depicted in Figure 1.2. Equation (1.2) enables us to leverage the PDoA, which incorporates parameters such as the speed of light denoted by c, the distance between the antennas within the array denoted as l, and the central frequency of the UWB channel represented by f, to calculate the angle [15]:

$$\alpha = \arcsin \frac{\Delta\phi c}{2\pi l f}. \tag{1.2}$$

1.3 Problem Statement

The aim of this thesis project is to create a method for finding the location of a UWB tag indoors using just one UWB anchor, specifically based on the NXP

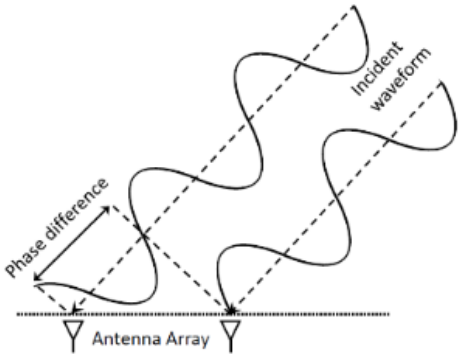

Figure 1.2: **Phase Difference of Arrival (adapted from [46]).**

SR150/SR040 chipsets. To determine the tag's position, we'll need to figure out both its distance from the anchor and its angle in relation to it. The idea of estimating position with a single anchor hasn't received much attention in academic research, especially when compared to systems with multiple anchors. This approach offers the potential to develop location setups that require fewer resources and are more cost-effective. As of writing this thesis, there hasn't been any published work on using a single anchor with these chipsets for localization.

1.3.1 Research Questions

The research questions we want to answer in the thesis project are as follows:

1. Is it possible to determine the distances between the virtual anchors and tag based on the Channel Impulse Response (CIR) that is determined from the antennas of the anchor and subsequently calculate the location of the tag?

2. Can the second antenna enhance the range estimate of the LOS and VAs, which subsequently improves the location accuracy of the tag?

1.3.2 Research Objective

The objective of this research is to analyze how UWB systems respond to multipath reflections within an indoor environment. While it is typically desirable to avoid multipath reflections when localizing UWB sensors, this research intentionally leverages these reflections to enhance the localization accuracy of UWB tags. Specifically, a localization method should be developed to utilize multipath reflections for accurately locating tags using a single UWB anchor.

1.3.3 Research Challenges

In the course of researching various methods for localizing UWB tags using a single anchor, three major challenges emerged, summarized as follows: Firstly,

the tags must be localized with only one anchor. Secondly, the method should be resilient to additional reflections that are encountered apart from the reflections from desirable sources. Lastly, a method should be developed that can localize the tags without relying on training data. The research challenges of this thesis are formulated as follows:

1. *Localize UWB tags using a single anchor.* While extensive research exists on localizing UWB tags using multiple anchors, the use of a single anchor, particularly in large indoor spaces, is challenging and has not received comparative attention.

2. *Resilient to extra reflections.* The CIR received at the anchor contains multiple reflections, making it challenging to estimate the source of each reflection. A method must be developed to identify and utilize reflections from desirable sources.

3. *Localize without training data.* Much of the existing research relies on training data to build machine learning models for tag localization. This research aims to develop a method that does not depend on training data, as it complicates the process of localization in different environments with varying sources of reflection.

1.3.4 Research Contributions

The following list summarizes the contributions made in this thesis:

1. An in-depth review of existing literature on UWB localization in indoor environments.

2. Analysis of various mathematical methods for approximating locations using equations.

3. Development of simulations that closely replicate the conditions present in the testbed setup to analyze how the Likelihood, Algebraic, and fminsearch methods respond.

4. Establishment of a data collection environment for gathering CIR data from the anchor, strategically positioned near one or more MPCs, facilitating the creation of virtual anchors to aid in tag localization.

5. Generation of a dataset comprising measurement data from the Murata NXP SR150 evaluation board in an indoor environment with single and double multipath components to induce reflections.

6. Pairing the collected dataset with ground truth distance and angle information, providing a basis for algorithm comparisons.

1.4 Thesis Structure

This thesis aims to provide an overview of the research process behind the development of localization methods for UWB tags in an indoor environment. The structure of the thesis is outlined as follows:

1. *Introduction* provides an overview of UWB technology and outlines the problem statement.

2. *Related Work* reviews the state-of-the-art research on indoor location using UWB and other similar techniques.

3. *System Design* describes the system architecture, the hardware used for data collection and discusses the different methods identified for localizing UWB tags.

4. *Simulation Evaluation* details the creation of the simulation environment and presents the results obtained when simulating UWB tags and anchors within it.

5. *Testbed Evaluation* outlines the data collection process and analyzes the results obtained using different localization methods.

6. *Conclusion* summarizes the findings of the thesis and discusses potential avenues for future research to further enhance UWB localization using single anchors and explores various applications that can be developed.

Chapter 2

Related Work

This chapter presents the findings derived from a comprehensive review of existing research and previous studies conducted by researchers in the field.

2.1 Indoor Localization

Indoor localization is the process by which an electronic device is located within an indoor environment, where technologies such as GPS fail to function effectively. Several technologies have been identified for indoor localization, including Inertial Navigation Systems (INS), sound-based methods, optical systems, Radio Frequency (RF) methods, and Radio Frequency Identification (RFID). This section is structured to first discuss the various available techniques for indoor localization, followed by examination of RF-based localization methods.

2.1.1 Indoor Localization Techniques

The following techniques have been identified for indoor localization:

1. *INS* technology utilizes sensors such as accelerometers, gyroscopes, and magnetometers to estimate the location of a device [18, 4, 43]. In [11], the use of these sensors within smartphones to localize the device while in motion is discussed. However, this method suffers from occasional drift. To counteract this, data from iBeacons is utilized for corrections. Despite these corrections, the method still exhibits errors ranging from 1 to 2 meters.

2. *Ultrasonic Navigation System* is used for indoor localization by emitting ultrasound signals and determining the location based on the time of flight of these signals [7, 17]. In [6] a novel approach is presented that utilizes reflection data to assist in localization, achieving an average error of 15 centimeters.

3. *Optical* data can be utilized for indoor localization, primarily through two technologies: Infrared communication and Visible Light Communication (VLC) [5, 40, 2]. In [20], Visible Light Positioning (VLP) for robots in indoor environments is discussed, employing efficient LED-ID detection to achieve localization accuracy of 1 cm.

4. *Radio Frequency (RF)* systems are the most widely used for indoor localization due to their low hardware cost and ability to cover larger areas [31]. Additionally, RF signals can penetrate through walls and human bodies, enhancing their effectiveness in various indoor environments [38].

2.1.2 RF based Localization Techniques

RF-based systems are widely used for indoor localization due to their low cost and ability to penetrate non-reflective objects such as walls and plastic. However, metallic objects are generally reflective and cause multipath reflections, which introduce significant noise into the localization data [23]. These systems can be designed to operate at various frequencies depending on the required coverage distance and resilience to different objects [31]. The following are the RF technologies quite widely being used for localization:

1. *Ultra-Wideband* (UWB) is a broadband technology that uses high-frequency pulses, resulting in short duration signals hence enabling to reduce multipath interference. These sensors typically return distance, RSSI, and angle data. This spatio-temporal data has been used in numerous studies to train neural networks for localizing UWB tags [44, 47, 15]. In [14], researchers successfully localized UWB tags on a robot in an industrial environment with an average error of 0.45 m.

2. *WiFi* is a widely popular networking technology used for communication over distances of several hundred meters and, in some cases, even kilometers [30, 45, 22]. Due to the extensive deployment of WiFi routers, they can be found in most buildings, enabling localization through techniques such as fingerprinting. However, WiFi lacks the ability to provide centimeter-level accuracy [29].

3. *Bluetooth Low Energy* (BLE) is a low-power, short-range communication technology [8, 33]. It is commonly used for localization in larger settings such as offices and shopping centers [35, 36]. In [37], researchers were able to localize BLE enabled smartphone using multiple BLE beacons, achieving an average error of 1.48 meters.

4. *Radio Frequency Identification* (RFID) operates on the principle of backscattering communication and can be utilized for indoor localization [10, 9]. In [32] researchers successfully localized vehicles indoors by combining sensor fusion with computer vision, achieving an accuracy of up to 1 centimeter.

5. Zigbee provides a power-efficient approach for indoor localization by using the Received Signal Strength (RSS) method to estimate distances between devices [38]. This method leverages low power consumption, making it suitable for various applications [21, 12]. In [16], the researchers employed neural networks to enhance localization accuracy, achieving an average precision of approximately 0.58 meters. This study demonstrates the potential of combining Zigbee's energy-efficient communication capabilities with advanced machine learning techniques to improve indoor positioning accuracy, thereby supporting a wide range of applications in smart environments, such as homes, offices, and industrial settings.

6. *LoRa* based positioning systems utilize the RSSI value to locate objects [24, 28]. Due to their long-range capability and minimal power consumption, these systems are desirable for long-range localization, even when using narrow bandwidth [1]. In [3] the authors are able to localize tags in a large university campus with a median error of 9 meters.

2.2 UWB

This section explores various UWB localization methods, which differ based on the number of UWB anchors deployed. It examines both multiple-anchor and single-anchor localization techniques. Following this, the section delves into the widely available hardware options for building UWB solutions.

2.2.1 Multi Anchor Systems

Most research into UWB technology focuses on multi-anchor networks like AnguLoc [23], which utilizes four anchors positioned at the corners of a room. Taking advantage of the dual antennas present on each anchor, AnguLoc calculates four AoAs, achieving decimeter-level accuracy. Similarly, ULoc [47] introduces a 3D localization system using eight strategically placed anchors, each equipped with four antennas. This system enhances localization accuracy to 3.6 centimeters but at the expense of deploying 32 antennas, rendering it cost-inefficient.

These systems exploit multiple anchors positioned strategically within a room to precisely locate tags. This indoor precision results from the controlled environment and the increased number of reflections utilized for more accurate triangulation and localization. Consequently, these systems find extensive application in scenarios requiring precise indoor positioning, such as asset tracking, navigation, and various smart home technologies.

Innovations in such systems primarily focus on scalability, latency reduction, and accuracy enhancement. For instance, [23] introduces a concurrent angle estimation system, allowing tags to receive multiple messages from anchors simultaneously using dual antennas. This substantially reduces the airtime required to locate a single tag, thereby increasing the maximum number of tags tracked by the system and extending the battery life of the tags by enabling a lower duty cycle. The system establishes a clear baseline performance, with angle estimation precision and a positioning 90th percentile error reported at 67 centimeters.

2.2.2 Single Anchor Systems

Our research focuses on single anchor systems, which typically receive less attention compared to multi-anchor systems due to their longer history and perceived limitations. At the time of writing, no research on the NXP SR150 chipsets for localization using single anchor methods could be found. However, notable research has been conducted using single anchor systems with other hardware. For instance, [15] delves into the Decawave/Qorvo DM1000 board, one of the most researched single anchor systems. This work elaborates on how UWB receivers can achieve path separation thanks to the large bandwidth and short duration

of UWB pulses. Additionally, [41] proposes a single anchor positioning system where tags send pulses quasi-simultaneously, allowing the anchor to activate its receiver only once. This increases scalability and efficiency, achieving a median positioning error of 7.5 cm and a 90th percentile error of 16.8 cm while tracking three tags concurrently.

Another significant study is SALMA [19], which utilizes a single anchor and the reflections generated by multipath fading in indoor environments. Although SALMA requires a floor plan, it achieves a median error below 8 cm and maintains an error below 20 cm for 90% of position estimates under Line-of-Sight (LOS) conditions. Similarly, [25] explores single anchor localization with floor plan information, yielding errors below 30 cm for 90 of location estimates. However, their evaluation area was relatively small, at 30x30 cm. Our research aims to expand the evaluation area significantly, approximately 4x5 meters, adapting one of the methods used in previous studies to explore its efficacy in a larger setting.

In [13], a single-anchor mechanism is outlined, focusing on a stationary tag. The study aims to localize the position of a human walking in an indoor environment, where environmental changes affect signal propagation between the tag and anchor. By collecting Channel Impulse Response (CIR) data and segregating it into amplitude and phase components, the study aims to classify different positions within the enclosed space based on these variations.

Extensive evaluation of various UWB evaluation boards and their performance characteristics was conducted in [39]. Based on the insights gleaned from this report, we have opted to advance with the Murata NXP SR150 evaluation board due to its exceptional performance surpassing other available boards in the market.

2.2.3 UWB Hardware Developments

Several hardware platforms are specifically engineered to interface UWB chips with microcontrollers. The following are some commercially available evaluation boards:

1. *Mobile Knowledge Evaluation Board*: This board features three antennas positioned at the back, facilitating tag localization in a 3D space by utilizing azimuth and elevation angles [39].

2. *Murata NXP Evaluation Board*: This relatively new board, although not extensively utilized at the time of writing, outperforms the Mobile Knowledge board in terms of distance and angle data accuracy [39]. This board also consists of three antennas to localise the data in 3D space.

3. *Decawave Qorqo DW1000 Evaluation Board*: Among the most widely used evaluation boards for studying localization algorithms, this board employs two antennas to calculate AoA and generate CIR for both antennas [15].

2.3 Challenges in Indoor UWB Localization

A prevalent challenge encountered when employing UWB chipsets for indoor localization pertains to the inherent lack of calibration in the antennas within

these chipsets, resulting in inaccurate angle data derived from the Phase Difference of Arrival (PDoA). In many instances, this inaccuracy reaches a point where the angle data becomes entirely unreliable. Mitigating this challenge often necessitates the deployment of multiple UWB anchors. While this approach enhances tag localization accuracy, it introduces a twofold issue: escalated operational costs due to the increased number of anchors and the intricate task of synchronizing data from these multiple sources.

To address the dilemma of optimizing resource utilization, a promising solution lies in the adoption of virtual anchors. These virtual anchors function as surrogate anchor points, and their presence manifests through distinctive peaks observed beyond the Line-of-Sight (LOS) signal peaks. This innovative approach not only reduces costs but also offers a viable means to enhance the robustness of indoor localization systems.

Chapter 3

System Design

This chapter first presents the overall system architecture. Then, it introduces the different methods that have been proposed for localization using a single UWB anchor.

3.1 System Architecture

This section explains the high level structure of the system.

An overview of conducting a UWB ranging session and data acquisition is depicted in Figure 3.1. Following initiation of a ranging session between a tag

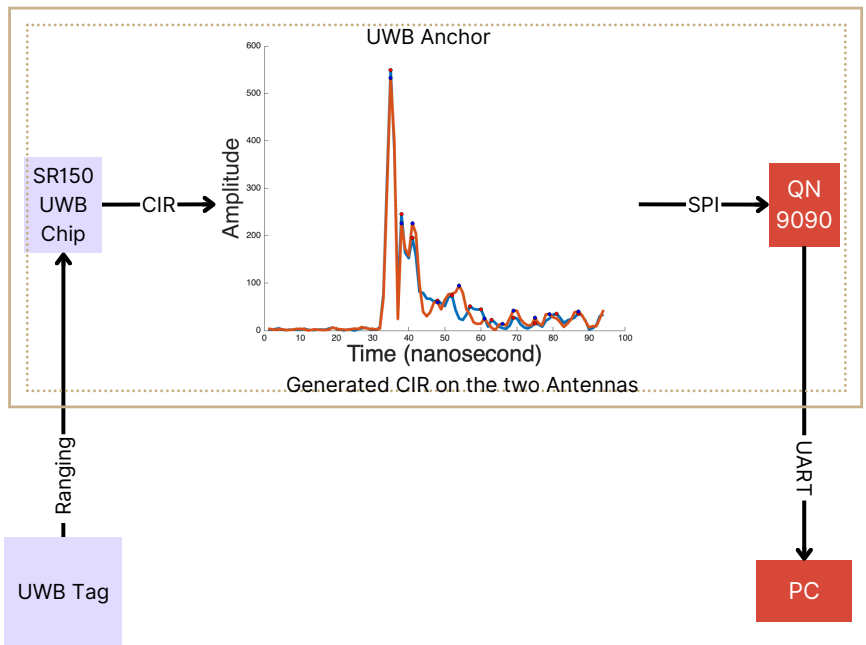

Figure 3.1: **High-level design of the data gathering process when a ranging session between the anchor and tag takes place.**

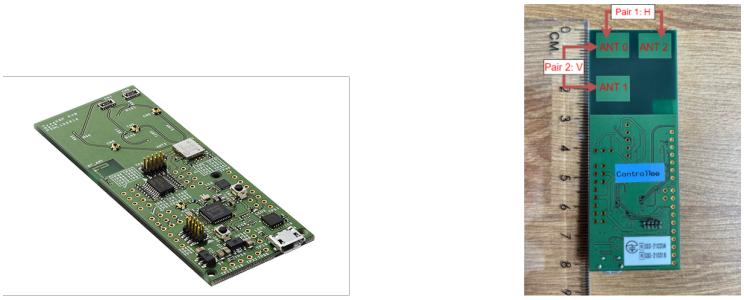

(a) **Front Display** (b) **Back Display**

Figure 3.2: **Murata NXP150 UWB Evaluation Board.**

and anchor, the Channel Impulse Response (CIR) received on the two antennas of the anchors is recorded within the registers of the SR150 UWB chip. Subsequently, the CIR data is communicated to the microcontroller via SPI communication. The data is then transmitted to the PC via UART communication, where it undergoes processing to determine the location of the tag and compare it with the ground truth.

3.1.1 Evaluation Boards

The evaluation board used for this research was the Murata NXP SR150 Rev 3.3 and Rev 4.1 revisions of the board. These boards make use of the NXP SR150 UWB chipset and NXP QN9090 micro-controller. The SR150 UWB chip communicates with the micro-controller using SPI communication. The Software Development Kit provided by Murata for it can modified according to the use case. These boards are equipped with 3 antennas separated by a distance of 1.6 centimeters. This distance between the antennas is carefully decided as these boards when used with channel 9 (8 GHz frequency), the distance between the antennas should be half the wavelength. This enables in calculation of angle of arrival using the phase angles obtained from the two antennas. The boards can even be programmed to work with different frequencies by selecting the different channels, such as 5, 6, 8 and 9. But the board has been optimised to work with channels 5 and 9. The three antennas form 2 pairs of antennas as shown in Figure 3.2a. The horizontal pair antennas return the azimuth angle where as the vertical pair of antennas give the elevation angle. The board is equipped with a micro-usb port to power it. It is not possible to communicate with the SR150 chip directly, as communication has to take place via the microcontroller.

3.1.2 Anchors

Anchor are the boards which receive the UWB signals that are transmitted by UWB tags. To configure the boards to act as anchors they have be programmed into controllee mode. There are several configuration settings that have to be configured for successful ranging between the two UWB devices, like the channel the tags communicate on, ranging interval, the STS (Scrambling Timestamp Sequence), etc. The anchor boards receive the signal on two or more antennas to make use of the phase information to calculate the AoA.

3.1.3 Tag

Tags are the boards that transmit the signals for the anchors to receive it. The boards have to configured to be in the controller mode. The tags make use of just a single antenna to transmit the signal. Any of the three antennas present on the board can be configured to transmit the signal.

During the initial phase, known as the discovery phase, the tag periodically transmits blink messages and then enters a sleep state. When the anchor receives the blink message, it decides to pair with the tag and sends a ranging configuration message. The tag, upon receiving the ranging message, establishes a pairing with the anchor. Subsequently, the two devices engage in periodic ranging to calculate distances, PDoA, CIR, and other relevant parameters.

3.1.4 Software

The board can be programmed to return various ranging variables from the such as CIR and SNR. The Murata board works on the NXP middleware directly by default. The middleware does not output these variables as standard. The middleware has to be programmed to send extra notifications apart from the standard distance and angle data. The SR150 in turn returns so-called notifications to the QN9090 which contain data relevant to the type of notification. Examples of such notification types that are present are Ranging data received, data transmitted, RFrame data, CIR logging, etc. By changing what the middleware does when it receives such a notification, the board was able to output all of the variables that were required to the serial line output connected to micro-usb port of the evaluation board. The data flow can be observed as shown in Figure 3.3.

A Python script was custom-developed to capture the variables transmitted via the serial line over USB on a PC. This script aggregated all variables associated with a single measurement into a unified line within a CSV file, facilitating data processing. Table 3.1 outlines the variables recorded by the script.

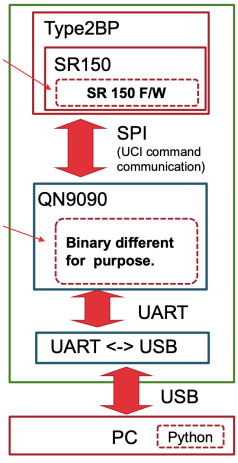

Figure 3.3: **Data flow between the different components available on the evaluation board.**

Table 3.1: **List of variables returned via notifications by the evaluation board after modifying the middleware software.**

Variable Name	**Data Returned**
Distance	Distance reported by the chip in centimeters.
Azimuth	Azimuth angle in degrees
AzimuthFOM	Azimuth estimation figure of merit
Elevation	Elevation angle in degrees
ElevationFOM	Elevation estimation figure of merit
RSSIrx1	Received Signal Strength Indicator Receiver 1
RSSIrx2	Received Signal Strength Indicator Receiver 2
Nlos	If ranging happens in LOS or NLOS
PdoaFirst	Estimation of phase difference in degrees from antenna pair 1
PdoaFirstIndex	CIR index estimate at which PDoaFirst has been detected
PdoaSecond	Estimation of phase difference in degrees from antenna pair 2
PdoaSecondIndex	CIR index estimate at which PDoaSecond has been detected
CIR0complexList	CIR samples from antenna pair 1
CIR1complexList	CIR samples from antenna pair 2
SNRMainPath	Signal-to-Noise Ratio (SNR) of the main path in dB
SNRFirstPath	SNR of the first path in dB
RSSI	Received Signal Strength Indicator (RSSI) in dB
Noise Variance	Noise variance in the CIR.
AoAPhase	AoA Phase in degrees

3.1.5 Channel Impulse Response

The CIR tells us about the received power of the signal during a UWB ranging session. Figure 3.5 shows the phase of the received signal and Figure 3.4 shows the amplitude. In the context of UWB communication systems, the CIR refers to the characterization of the channel's behavior over time. The impulse response describes how the channel responds to a short-duration pulse transmitted through it. In UWB systems, pulses with very short duration (typically in the nanosecond range) are used for communication.

Equation 3.1 from [25] characterizes the CIR of the propagation medium. The deterministic MPC indexed by $k \in K$ can be calculated as follows:

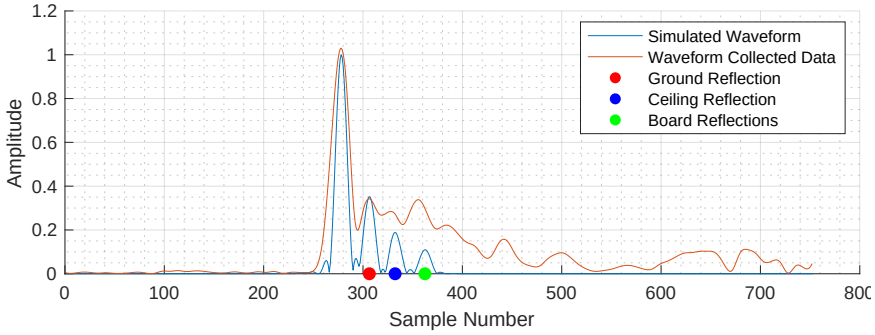

Figure 3.4: **The Amplitude of the Channel Impulse Response.**

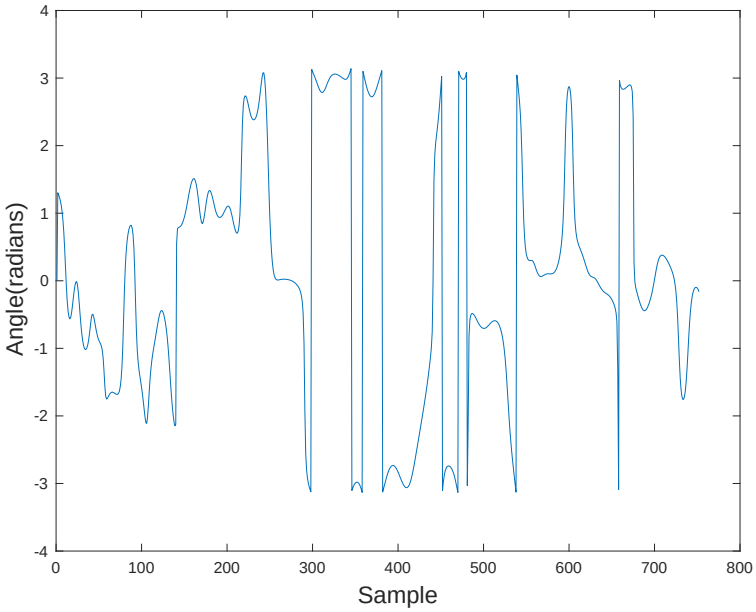

Figure 3.5: **The Phase of the Channel Impulse Response.**

$$h(t) = \sum_{k \epsilon K} \alpha_k \delta(t - \tau_k) + \nu(t), \tag{3.1}$$

where each MPC is defined by its complex-valued amplitude α_k and delay τ_k, with $\delta(t)$ denoting the Dirac delta function. The second term denoted as diffuse multipath (DM) $\nu(t)$, models scattering phenomena originating from small objects.

The received signal as a function of $h(t)$ can be written as follows:

$$r_{\text{received}}(t) = s(t) * h(t - t_0) + w(t), \tag{3.2}$$

where $*$ denotes the convolution operator, $s(t)$ represents the energy normalised, t_0 is the CIR offset and $w(t)$ is the additive White Gaussian noise.

The initial peak in Figure 3.4 corresponds to the LOS path, while subsequent peaks depict reflections occurring in the surrounding environment. Notably, the red and blue dots in the figure symbolize ground and ceiling reflections, respectively.

The CIR comprises complex data, encompassing both an imaginary and a real part. The amplitude of the CIR signifies the magnitude or strength of the received signal, while the phase contains the angle information. The CIR can be thought of as an array of complex elements. Each element of the array can be represented as

$$CIR(:) = x + iy. \tag{3.3}$$

The magnitude of each element of the CIR can be calculated as follows:

$$Mag(CIR(:)) = \sqrt{x^2 + y^2}. \tag{3.4}$$

The phase angle is calculated as follows:

$$Phase(CIR(:)) = \tan^{-1}\left(\frac{y}{x}\right). \tag{3.5}$$

The CIR is generated on the UWB sensor whenever a ranging session takes place between two sensors.

3.2 Virtual Anchors

In Figure 3.6, multiple signal propagation paths between the transmitter and the receiver are shown. The green path signifies the LOS direct path, while the red path represents the reflected signal bouncing off the wall. The virtual anchors emulate the signal's trajectory as if it were traversing in a straight line from an anchor that represents the reflected signal. The virtual anchor position calculation is explained in [26].

We describe the position and orientation of the wall segment S by the vectors p_S and $l_S e_S$, respectively, with l_S as length and e_S as unit vector indicating the direction of wall segment as shown in Figure 3.7. The closest distance between S and agent m is calculated by the projection of $\mathbf{p}_S - \mathbf{p}^{(m)}$ onto $\mathbf{R}_{\frac{\pi}{2}}\mathbf{e}_S$ where $\mathbf{R}_{\frac{\pi}{2}}$ denotes the rotation matrix denoted by the following equations:

$$\mathbf{R}_{\frac{\pi}{2}} = \begin{bmatrix} \cos(\frac{\pi}{2}) & -\sin(\frac{\pi}{2}) \\ \sin(\frac{\pi}{2}) & \cos(\frac{\pi}{2}) \end{bmatrix}, \tag{3.6}$$

$$d_{m,s} = (\mathbf{p}_S - \mathbf{p}^{(m)})^T \mathbf{R}_{\frac{\pi}{2}}\mathbf{e}_S. \tag{3.7}$$

The VA position $\mathbf{p}_2^{(m)}$ is calculated according to

$$\mathbf{p}_2^{(m)} = \mathbf{p}^{(m)} + 2d_{m,S}\mathbf{R}_{\frac{\pi}{2}}\mathbf{e}_S. \tag{3.8}$$

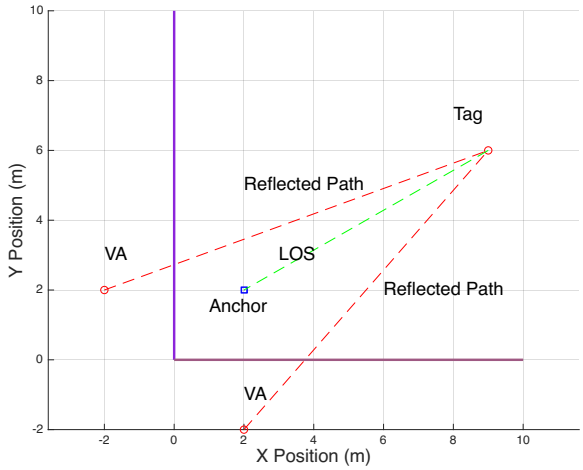

Figure 3.6: **Virtual Anchor representation when there are two Multipath Components present.**

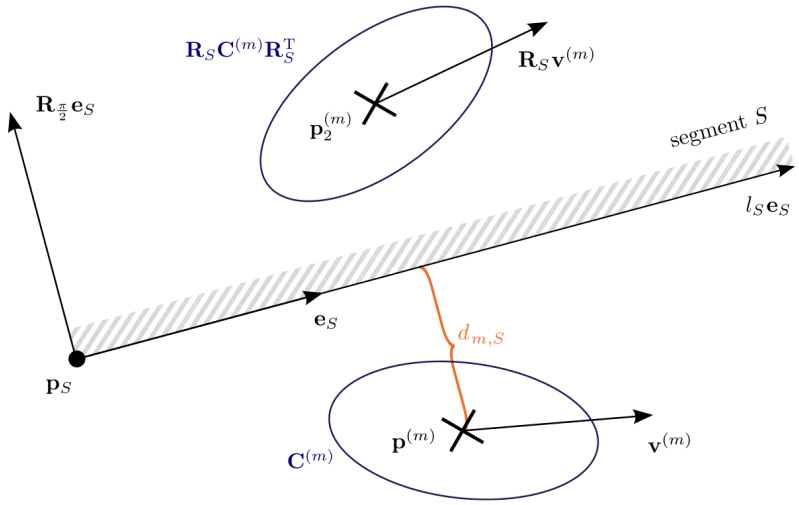

Figure 3.7: **Illustration of agent position $p^{(m)}$. The wall segment's orientation, indicated by p^S and e^S help in calculating the position of the virtual anchor $p_2^{(m)}$**

.

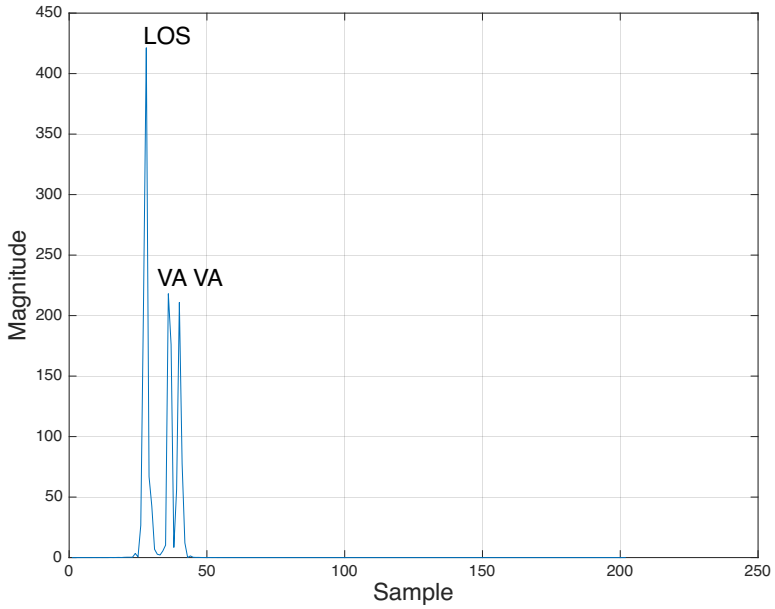

Figure 3.8: **Simulated signal received at the anchor end showing the LOS and MPC peaks.**

In Figure 3.8 we can see the received signal at the anchor end based on the scenario described in Figure 3.6 (simulated). The first peak corresponds to the LOS signal and the subsequent peaks correspond to the MPC's. Each sample

index corresponds to time interval of 1 ns. Since the UWB chipsets return the distance between the anchor and tag it is possible to calculate the distance between the tag and each of the virtual anchors. Distance between VA's and and tag can be calculated as follows:

$$D_{\mathrm{MPC}} = D_{\mathrm{LOS}} + \frac{(I_{\mathrm{MPC}} - I_{\mathrm{LOS}}) * c}{f}, \tag{3.9}$$

where c represents the speed of light, f is the frequency at which the signal is transmitted and I is the index of the peak. These distances are used in Algebraic method and Fminsearch method.

3.3 Proposed Localization Methods

This section discusses three proposed methods for localization. The first method is the likelihood method, followed by the algebraic method and the fminsearch method. The details of these methods are as follows:

3.3.1 Likelihood Method

In employing the Likelihood Method, we follow a process in which we sample 100 data points distributed within a radius equivalent to the distance between the anchor and the tag. The distance information is given to us by the sensor when we will try to localise the tag in the real world setting, currently we use euclidean distance to calculate the radius around which these points are

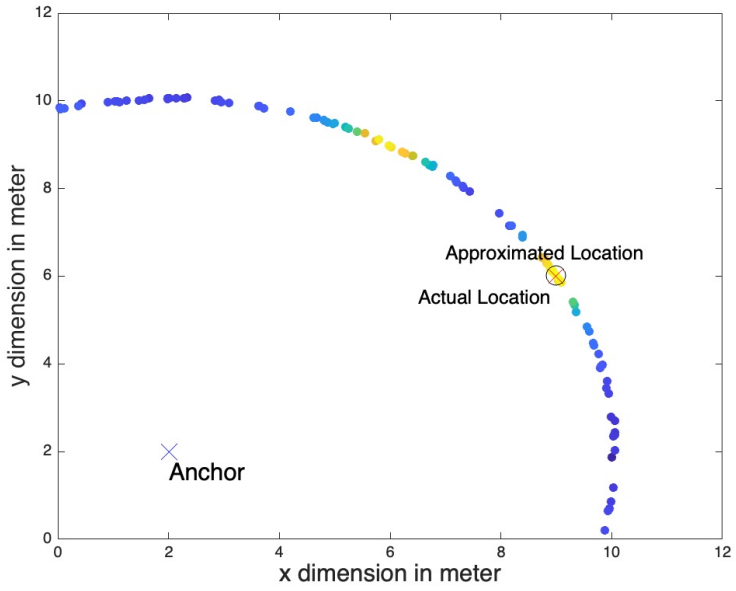

Figure 3.9: **Approximated tag locations with the likelihood method.**

sampled. Subsequently, we perform a detailed analysis to calculate the likelihood associated with each of these data points, indicating the probability that each point represents the actual location of the tag. This analysis is conducted by leveraging the information contained within the CIR data.

In Equation (3.10), the variable r represents the received complex-valued CIR in vector notation, which is equal to the summation of time-shifted amplitude and DM (diffuse multipath).

$$r = \sum_{k \epsilon K} \alpha_k s(\tau_k) + w, \tag{3.10}$$

$$r = S(\tau)\alpha + w. \tag{3.11}$$

We simplify the channel model by approximating the DM as a white, stationary Gaussian process. The likelihood function of Equation (3.11) with respect to delay τ and amplitudes is as follows:

$$p(r \mid \tau, \alpha) \propto \exp(- \left\| r - S(t)\alpha \right\|^2). \tag{3.12}$$

In simplification of Equation (3.12), a predefined value of τ is utilized, and the amplitudes are computed using the linear least squares solution as follows:

$$\hat{\alpha} = (S(\tau)^H S(\tau))^{-1} S(\tau)^H r, \tag{3.13}$$

where the superscript $(.)^H$ denotes the Hermitian transpose. To maximize Equation (3.13) with respect to the agent position p, the deterministic MPC delays τ are substituted with p and $\{a_k\}_{k \epsilon K}$. Then the ML (Maximum Likelihood) can be reformulated and the ML solution of the agent position estimate p as follows:

$$\hat{p} = \text{argmax}_{p \epsilon P} p(r \mid p, \{a_k\}\, k \epsilon K). \tag{3.14}$$

We approximate Equation (3.14) by considering I sampling points. The sampling points are uniformly distributed around with a radius that is Gaussian with mean d as follows:

$$d^{(i)} \sim \mathbb{N}(d, \sigma^2), \tag{3.15}$$

$$\phi^{(i)} \sim \angle(0, 2\pi), \tag{3.16}$$

$$p^{(i)} = [d^{(i)} cos(\phi^i), d^{(i)} sin(\phi^i)]^T + a. \tag{3.17}$$

In Equation (3.15) and Equation (3.16) represent the Gaussian and Uniform distribution and σ^2 is the range variance. Sampling points which lie outside the area of interest (i.e. outside the room) are rejected.

In Figure 3.9, 100 points are distributed across potential locations within the room, each adhering to a specified radius. The likelihood for each of these points is determined by analyzing the Channel Impulse Response of the collected data. Subsequently, the point exhibiting the highest likelihood is singled.

Detailed explanation can be found in [25] about the procedure of localising the tag using the likelihood method.

3.3.2 Algebraic

In this method we make use of the peak information in the CIR and approximate the peak timings to distances. The distance can be calculated using the sample time of the peak multiplied with the speed of light as the signals travel at the speed of light.

After obtaining the distances we make use of the multilateration equations to solve for the position of the tag. The general expression of multilateration equations is as follows:

$$\begin{bmatrix} 1 & -2x_1 & -2y_1 & -2z_1 \\ 1 & -2x_2 & -2y_2 & -2z_2 \\ 1 & -2x_3 & -2y_3 & -2z_3 \\ \vdots & \vdots & \vdots & \vdots \\ 1 & -2x_n & -2y_n & -2z_n \end{bmatrix} \begin{bmatrix} x^2+y^2+z^2 \\ x \\ y \\ z \end{bmatrix} = \begin{bmatrix} s_1^2 - x_1^2 - y_1^2 - z_1^2 \\ s_2^2 - x_2^2 - y_2^2 - z_2^2 \\ s_3^2 - x_3^2 - y_3^2 - z_3^2 \\ \vdots \\ s_n^2 - x_n^2 - y_n^2 - z_n^2 \end{bmatrix}. \tag{3.18}$$

Equation (3.18) represents the expression in a 3D environment. For our experiment, we consider a 2D environment so we can ignore the z terms.

Trilateration (2 Walls)

This method necessitates a specific setup that includes the presence of two walls, resulting in the appearance of two additional peaks within the CIR in addition to the LOS peak. By leveraging the information extracted from these CIR peaks, distances between the virtual anchors (or anchors) and the tag are computed.

These distance measurements, in turn, form the basis for the derivation of three sets of algebraic equations. These equations are used in estimating the precise positions of the tag within the designated area. Detailed explanation of this method can be found in [34].

Bilateration (1 Wall)

This method closely resembles the trilateration approach, differing primarily in the number of walls considered in this experiment utilizing only one MPC. Therefore we get two peaks in the CIR from the LOS and reflected signal from one MPC. In Figure 3.10, two circles with centers P and Q and radii R_p and R_q can be seen. These circles intersect at points A and B. Points P and Q correspond to the locations of the anchor and virtual anchor, with their radii representing distances from the anchors to the tag. Points A and B signify potential tag locations. The equations for circles P and Q can be defined below:

$$(x - x_p)^2 + (y - y_p)^2 = R_p^2, \tag{3.19}$$

$$(x - x_q)^2 + (y - y_q)^2 = R_q^2. \tag{3.20}$$

The line passing through points A and B is defined by

$$y = mx + c, \tag{3.21}$$

where m and c denote the slope and y intercept respectively. Values for m and c can be calculated as follows:

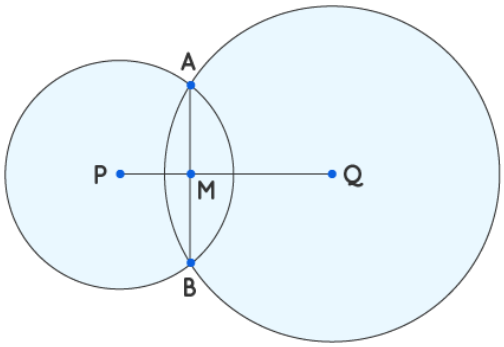

Figure 3.10: **Visualisation of the Algebraic method.**

$$m = \frac{x_q - x_p}{y_p - y_q}, \tag{3.22}$$

$$c = \frac{x_p^2 + y_p^2 + R_q^2 - (x_q^2 + y_q^2 + R_p^2)}{2(y_p - y_q)}. \tag{3.23}$$

It is possible to eliminate either point A or B if they fall outside the simulation environment. By substituting (3.21) in (3.19) or (3.20) it is possible to calculate the coordinates of points A and B.

3.3.3 F-min search (Nelder-Mead Simplex Algorithm)

In this specific localization method the tag's location is determined by extracting the distance information from the CIR between the tag and virtual anchor (or anchor).

Fminseach makes use of the Nelder-Mead simplex algorithm as described in [27]. This approach is employed to optimize the estimation of the tag's position by leveraging distance data derived from the CIR. Within Matlab, the **fminsearch** function is integral to this process. This function takes as input a position equation describing the tag's location based on distances extracted from the CIR, along with an initial guess for the tag's position at the centre of the experimental environment. The **fminsearch** function iteratively minimizes the error with respect to the initial position, calculating new positions until convergence is achieved, i.e., the newly calculated position matches the previous one.

Explanation of Nelder-Mead Simplex Algorithm

Following is the explanation of the Nelder-Mead Simplex Algorithm:

1. **Initialization**: Start with $n + 1$ initial points $x_1, x_2, \cdots, x_{n+1}$ in n-dimensional space. These points form the vertices of the initial simplex.

2. **Evaluation**: Evaluate the objective function f at each vertex of the simplex to get $f(x_1), f(x_2), \cdots, f(x_{n+1})$.

3. **Ordering**: Order the vertices such that $f(x_1) \leq f(x_2) \leq \cdots \leq f(x_{n+1})$.

4. **Reflection**: Compute the centroid $\bar{x}$ of the n best vertices (excluding the worst point x_{n+1}). Reflect the worst point x_{n+1} through the centroid to get the reflection point x_r:

$$x_r = \bar{x} + \alpha(\bar{x} - x_{n+1}),$$

where α is the reflection coefficient, typically set to 1.

Evaluate $f(x_r)$:

- If $f(x_1) \leq f(x_r) < f(x_n)$, accept x_r and replace x_{n+1} with x_r.

5. **Expansion**: If $f(x_r) < f(x_1)$, compute an expanded point x_e:

$$x_e = \bar{x} + \gamma(x_r - \bar{x}),$$

where γ is the expansion coefficient, typically set to 2.

Calculate the value of $f(x_e)$:

- If $f(x_e) < f(x_r)$, accept x_e and replace x_{n+1} with x_e.
- Otherwise, accept x_r and replace x_{n+1} with x_r.

6. **Contraction**: If $f(x_r) \geq f(x_n)$, perform a contraction:

- Outside contraction (if $f(x_n) \leq f(x_r) < f(x_{n+1})$):

$$x_c = \bar{x} + \beta(x_r - \bar{x})$$

- Inside contraction (if $f(x_r) \geq f(x_{n+1})$):

$$x_c = \bar{x} - \beta(\bar{x} - x_{n+1}),$$

where β is the contraction coefficient, typically set to 0.5.

Calculate the value $f(x_c)$:

- If $f(x_c) < f(x_{n+1})$, accept x_c and replace x_{n+1} with x_c.
- Otherwise, perform a shrink operation.

7. **Shrink**: If no improvement is made by reflection, expansion, or contraction, shrink the simplex towards the best point x_1:

$$x_i = x_1 + \delta(x_i - x_1) \quad \text{for} \quad i = 2, 3, \cdots, n+1,$$

where δ is the shrinkage coefficient, typically set to 0.5.

8. **Iteration**: Repeat the process from step 2 until the termination criteria are met, which could be a predefined number of iterations, a threshold for the change in function value, or the size of the simplex.

Usage of fminseach method in localization

Below is the explanation of using the fminseach method for localization in Matlab.

1. **Initialize**: Assign an initial position of the tag. It can be the centre of the environmental setup. If the environmental setup has an area of 10×10, then the initial position can be set as $(5, 5)$. Also define the measured distances between the tag and anchors (& virtual anchors) extracted from the CIR.
$$pos = (x_0, y_0),$$
$$CIRdistance_k = D_k,\ k \epsilon K.$$

2. **Assign Anchor Positions**: Assign positions to the anchor and virtual anchors. K is the list of anchors and virtual anchors.
$$Anchor_k = (x_k, y_k),\ k \epsilon K.$$

3. **Define the distance function**: Describe the function that calculates the distances between the tag location and anchors based on the initial guess.
$$Distance_k(pos) = \sqrt{(Anchor_k - pos)^2}.$$

4. **Define the cost function**: The cost is the error (difference) between the measured distances from the CIR and distances obtained from the distance function.
$$Cost = \sum_{k=1}^{K} (Distance_k(pos) - CIRdistance_k)^2,\ k \in K.$$

5. **Run the Function**: Using the fminseach function in Matlab the location of the tag can be computed. It iteratively changes the initial guess location and measures the cost. It tries to reduce the cost and when the cost can no further be reduced it returns the final resultant location of the tag.

Chapter 4

Simulation Evaluation

This section presents the simulations carried out to evaluate our methods.

4.1 Simulation Environment

A simulation environment was established in Matlab to generate signals. This simulation comprises two distinct phases. In the initial phase, users have the flexibility to define the layout of walls and specify anchor positions. Additionally, the positions of virtual anchors are determined based on the specified anchor locations and the wall layout. Subsequently, the distances between the tag and both the anchors and virtual anchors are calculated. These distance measurements serve as the foundation for generating the transmission signal.

Moving on to the second phase of the simulation, we focus on the reception end. The anchor is responsible for receiving the transmission signal, resulting in the generation of a Channel Impulse Response (CIR). It's essential to note that each antenna of the anchor receives a unique CIR. This disparity arises from the physical separation of the antennas by half a wavelength, causing distinct responses to the incoming signal. The received signals are subsequently processed, incorporating setup information such as the positions of anchors, virtual anchors, and the distances between the tag and anchors.

4.2 Signal Generation at the Anchor

The transmitted signal is represented by a raised cosine pulse, defined by a 1.5-nanosecond time period and a beta value of 0.8. Our simulation incorporates 204 sample points. The raised cosine pulse, generated with these parameters, displays a peak at the center index (interpolated by 8 times). To depict the scenario with zero signal propagation time, the signal is left-shifted, placing the peak at index zero. The resulting signals are illustrated in Figures 4.1 and 4.2.

Subsequently, the signal undergoes an eight-fold up-sampling to enhance resolution. The signal undergoes a transformation to the frequency domain through the application of Fast Fourier Transform (FFT), yielding the function $S(w)$:

$$H(w) = \sum_{k \in K} \frac{1}{r^2} e^{ir2\pi \frac{f}{c}}. \tag{4.1}$$

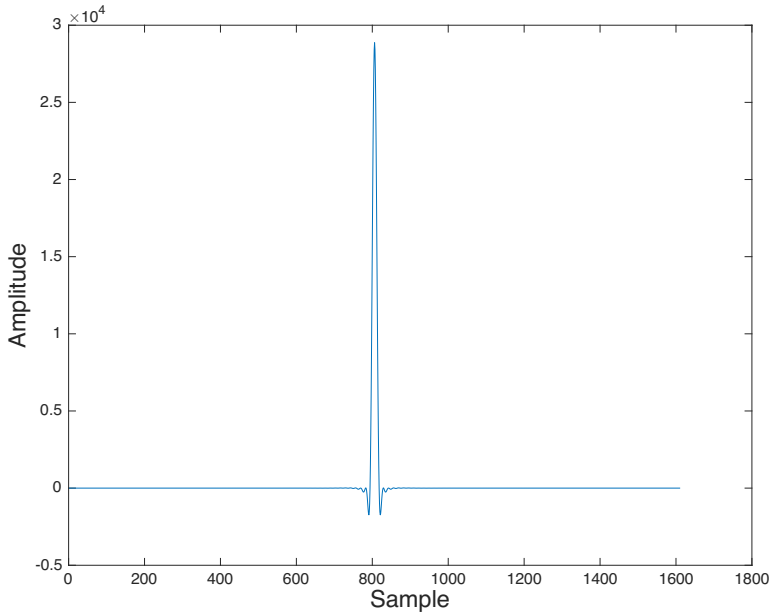

Figure 4.1: **Raised cosine pulse with peak at the centre index.**

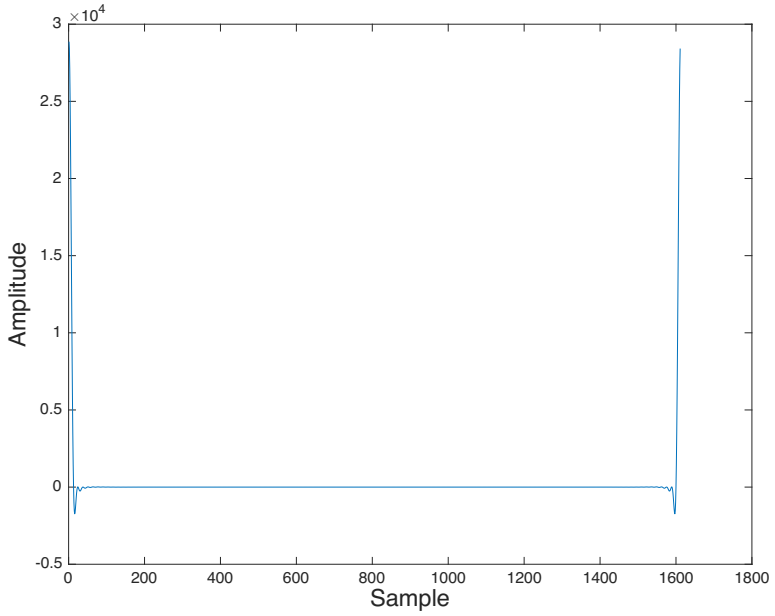

Figure 4.2: **Raised cosine pulse shifted to show zero distance traversed.**

Distances are computed between the tag and anchors, as well as virtual anchors. Subsequently, these distances are employed in Equation (4.1) to determine the propagation channel $H(w)$. In this equation, r denotes the distance between the tag and anchor, f represents the channel frequency at which the signal is transmitted, and c denotes the speed of light. Following the calculation

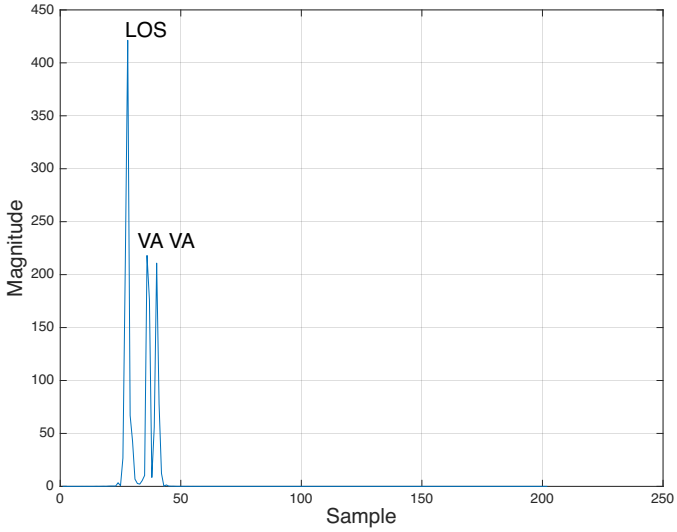

Figure 4.3: **Simulated signal received signal at the anchor end.**

of channel propagation for each Multipath Component (MPC), considering Line of Sight (LOS) and two virtual anchors, the results are summed.

In Equation (4.1), the term $1/r^2$ signifies the importance of path loss, reflecting the signal's decay in inverse proportion to the square of the distance as it propagates. On the other hand, the term $e^{ir2\pi\frac{f}{c}}$ introduces the time delay, as the signal experiences a delay corresponding to the distance r it must traverse.

To get the received signal, we perform the multiplication operation of $S(w)$ with $H(w)$, resulting in the received signal in the frequency domain as follows:

$$R(w) = S(w) * H(w) \tag{4.2}$$

Once $R(w)$ is computed, the Inverse Fourier Transform (IFFT) is applied to obtain the corresponding signal in the time domain, represented as $r(t)$. The signal for the scenario depicted in Figure 4.4 is shown in Figure 4.3. After the CIR is generated using IFFT, we can then use the generated signal to try to localise the location of the tag. Using the methods presented in Section 3.3 we try to find the tag's location and see which of these methods are effective.

4.3 Simulation in a Designated Grid Area

In this specific configuration, we define a region measuring 10×10 meters. The simulation environment can be visualised in Figure 4.4. An anchor is positioned at coordinates (2, 2), and a single wall is situated between the points (0, 0) and (0, 10) for single-wall simulations. For double-wall simulations, an additional wall is present between the points (0, 0) and (10, 0). Within this designated area, the tag is systematically placed at various locations, with a 0.1-meter spacing along both the x and y coordinates. Subsequently, we apply the localization methods mentioned earlier to determine the tag's location for each placement.

Since in our experiment we consider two antennas separated by distance of half the wavelength of the transmission signal we obtain two different CIR's.

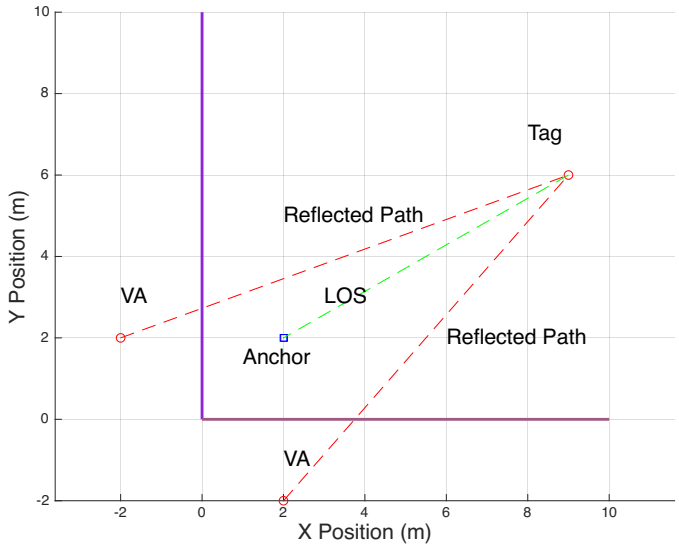

Figure 4.4: **Simulation Setup showing the two VA's, anchor and tag locations.**

Table 4.1: **Statistics for the different localization methods**

Method	Mean Error (m)		Standard Deviation		Locations Located %
	Ant 1	Ant 2	Ant 1	Ant 2	
Likelihood - 1 Wall	0.6267	0.6417	1.0505	1.0679	49.5
Likelihood - 2 walls	0.0996	0.0913	0.3178	0.2958	49.5
Likelihood - 3 walls	0.1147	0.1120	0.4027	0.4155	49.5
Algebraic - 1 wall	0.1489	0.1605	0.178	0.2068	74.0
Algebraic - 2 walls	0.116	0.1378	0.1649	0.221	36.0
Algebraic - 3 walls	0.0779	0.0998	0.0771	0.1714	23.0
Minimization - 1 Wall	0.237	0.2655	0.3053	0.9343	84.6
Minimization - 2 Walls	0.0799	0.1046	0.0909	0.1859	35.9
Minimization - 3 Walls	0.1318	0.1692	0.2104	0.2774	26.5

To evaluate the accuracy of the estimation, we calculate the error between the actual tag location and the estimated tag location at each point within the grid. The results of this simulation are presented in Table 4.1. The average error results, as depicted in Table 4.1, specifically consider data points with errors below 1 meter. This approach aims to provide a clearer understanding of algorithmic performance by excluding outliers with exceptionally high errors from the analysis. The CDF plots of these methods can be seen in Figures 4.5, 4.6 and 4.7.

Result - Likelihood

The results of the likelihood method are outlined in Table 4.1. This method typically yields around 2 potential locations, prompting the exclusion of the top half triangle of locations to refine location accuracy as seen in Figure 4.8. The occurrence of two potential locations in the upper and lower halves of

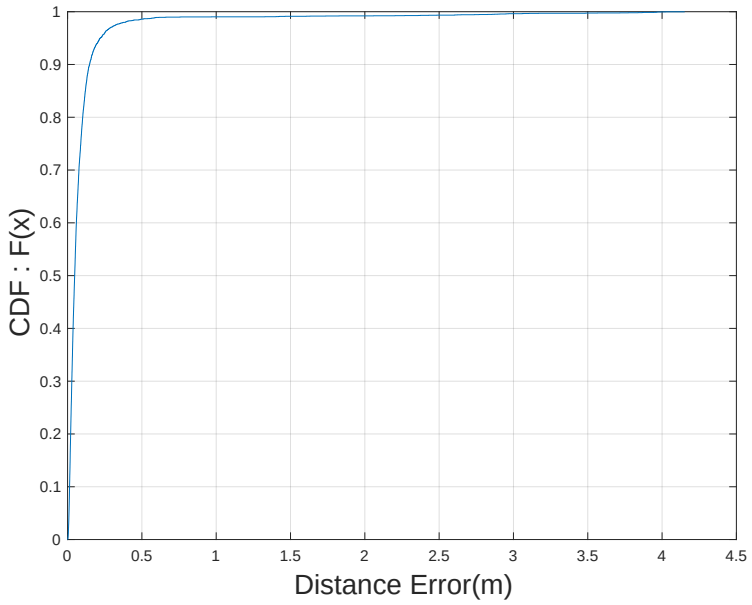

Figure 4.5: **Simulation results of the likelihood method (2 walls).**

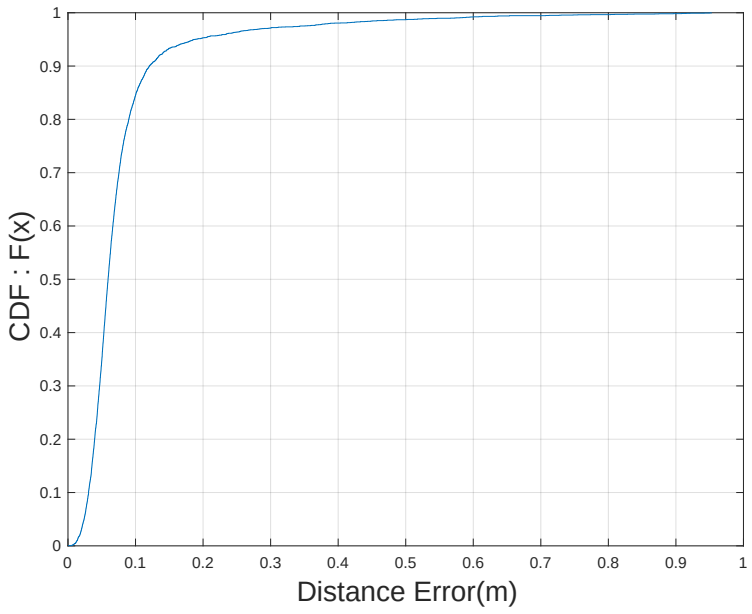

Figure 4.6: **Simulation results of the F-Min search method (2 walls).**

the possible locations is due to the fact that the CIR for the upper and lower halves are identical. The only difference is that MPC1 becomes MPC2 in the upper half, and vice versa. In this simulation, locations within the triangle defined by points (0,10), (10,0), and (10,10) are disregarded. The single-wall likelihood method demonstrates high error, as depicted in Figure 4.8. The error

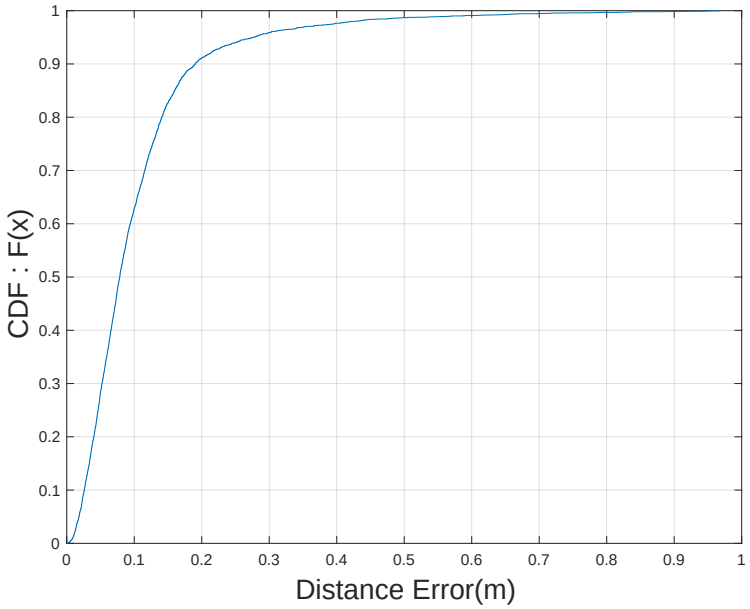

Figure 4.7: **Simulation results of the trilateration method (2 walls).**

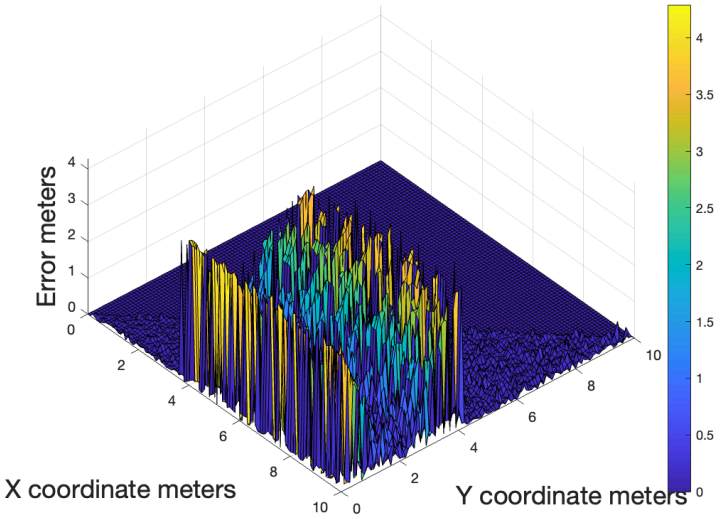

Figure 4.8: **Error calculated in the grid area simulation using the likelihood estimation method for localization (1 wall).**

is substantially reduced when the number of walls is increased to two, with only certain points at the edges of the simulation setup exhibiting high error, as illustrated in Figure 4.9. In the case of the three-wall setup shown in Figure 4.10, there is no significant improvement, yielding results similar to those of the two-wall setup.

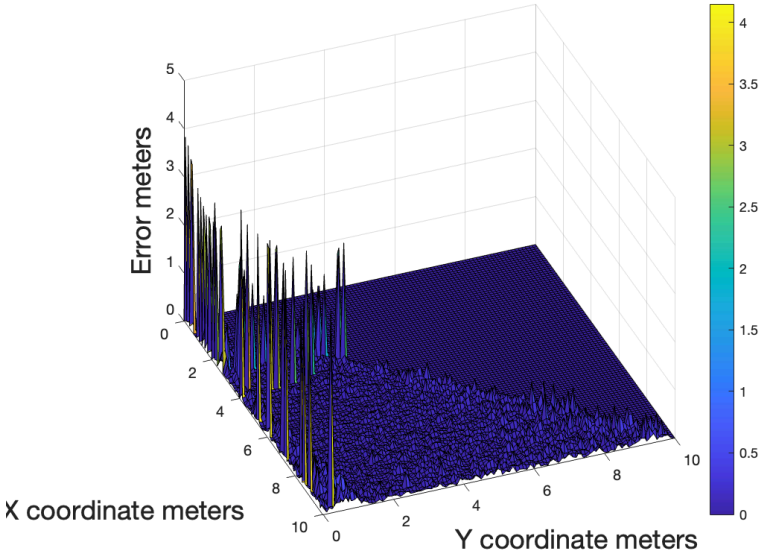

Figure 4.9: **Error calculated in the grid area simulation using the likelihood estimation method for localization (2 Walls).**

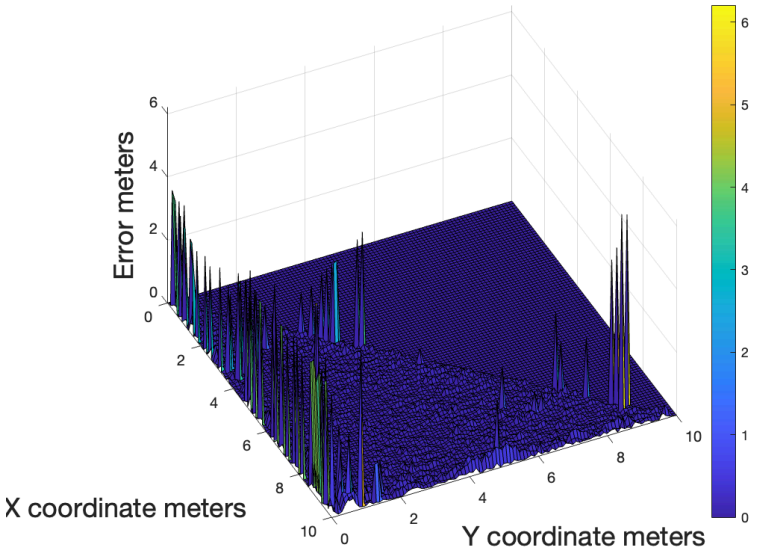

Figure 4.10: **Error calculated in the grid area simulation using the likelihood estimation method for localization (3 Walls).**

Result - Algebraic Two Walls (Trilateration)

This method relies on two walls to generate two virtual anchors , resulting in three identifiable peaks in the CIR under ideal conditions. However, in certain locations, MPC peaks may converge, preventing the detection of three distinct peaks and hindering the calculation of three distinct distances, leading to the failure of location detection.

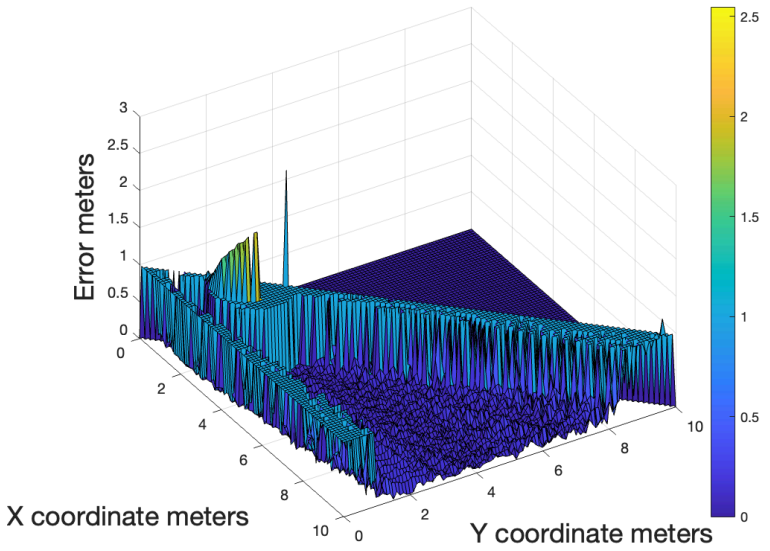

Figure 4.11: **Error calculated in the grid area simulation using the trilateration estimation method for localization.**

In Figure 4.11, the associated errors for different tag locations are depicted. Notably, along the line passing through points (0,0) and (10,10), the error is considerably high. This discrepancy arises when the tag is positioned along this line, equidistant from the two virtual anchors, causing the peaks from the two virtual anchors to converge.

Furthermore, similar to the likelihood method, this approach is constrained to detecting locations only in either the upper or lower half of the triangle within the square area grid setup this due to the fact that its difficult to detect whether MPC1 or MPC2 was responsible for the peak.

Result - Algebraic One Wall (Bilateration)

This method uses only one wall (1 MPC) and subsequently produces 2 peaks in the CIR of the receiver. Since in this method another wall is not present, convergence of peaks in the CIR is much lower than the trilateration method. The errors detected on average with this method are quite low, as can be seen from Figure 4.12 and Table 4.1. Detecting locations using this method yields relatively high results, even with only two distances (from anchor and virtual anchor). The distances can be employed to draw circles with the distances as the radii, and their intersections provide two potential locations. However, it is noteworthy that one of these locations consistently falls outside the simulation setup, simplifying the determination of the correct location.

Result - F-min Search

As indicated in Table 4.1 and Figure 4.13, the single-wall minimization method identifies a larger number of locations with relatively low average error. This is attributed to the presence of only one wall, causing the convergence of peaks to

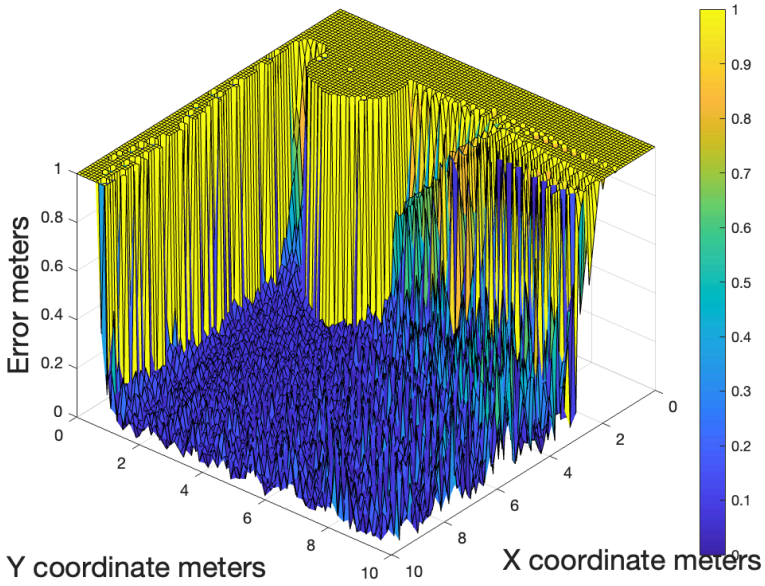

Figure 4.12: **Error calculated in the grid area simulation using the bilateration estimation method for localization.**

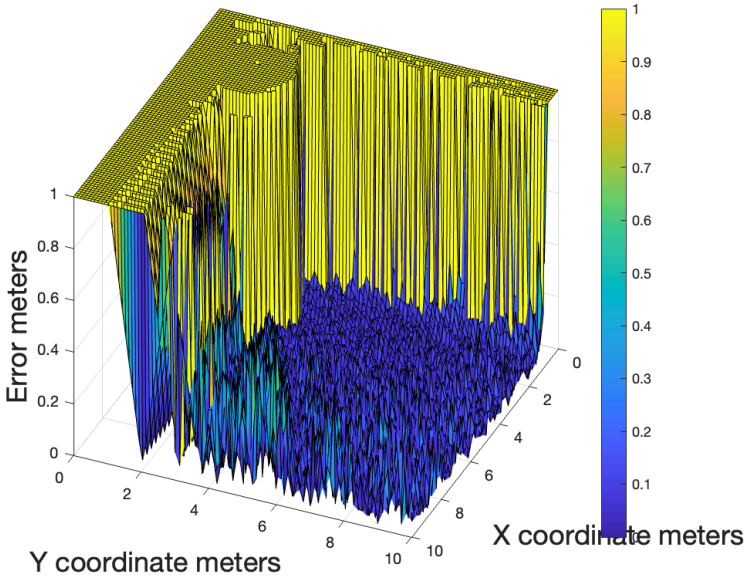

Figure 4.13: **Error calculated in the grid area simulation using the single-wall estimation method for F-min search localization.**

be limited. Consequently, this method is adopted to detect a greater number of locations. However, locations near the boundary exhibit higher error during localization. When employing two walls with this method, the mean error decreases, but the number of located locations drops to only 35%, as more peaks converge, leading to a more selective identification process can be seen in Figure 4.14.

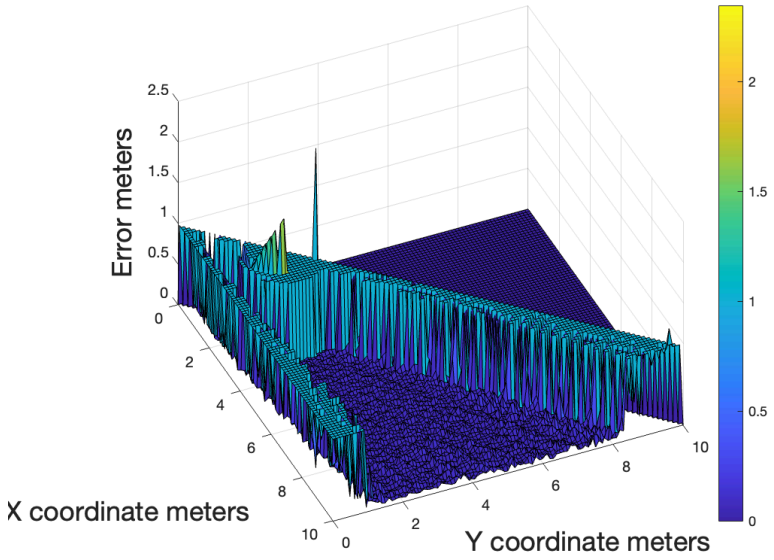

Figure 4.14: **Error calculated in the grid area simulation using the double-wall estimation method for F-min search localization.**

4.4 Impact of Anchor Locations

A simulation was conducted within a 6×6m grid area replicating the conditions of the test bed which will be discussed in the coming section. However, in this specific simulation, anchors were strategically placed at different positions on the grid, while the tag was positioned variably across the grid. The objective was to assess the generation of the CIR under these conditions. A scoring system was implemented based on the number of peaks generated and their distribution. A higher score was assigned when more well-separated peaks were observed. More information about the scoring algorithm can be found in Algorithm 1.

The scoring process involved evaluating the CIR for different tag locations, and the cumulative score was attributed to the corresponding anchor positions. The anchor's location was systematically altered, and the entire experiment was repeated across the entire grid during the simulation.

CIRs were generated considering the potential presence of ground and ceiling reflections in the environment. Given the existence of a single wall in this simulation, a total of four peaks could be expected, taking into account ceiling, ground, wall reflections and the LOS signal.

Figures 4.15 clearly indicates that the highest scores are attained when the tag is positioned at coordinates (3,0). Therefore at this specific location for the anchor we have a higher probability of yielding optimal results when determining tags location.

Algorithm 1 Simulation and Scoring for various anchor positions

Initialize grid parameters and simulation conditions.
for $anchor(x_a, y_a)$ **do**
  $totalScore(x_a, y_a) \leftarrow 0$
  for $tag(x_t, y_t)$ **do**
    $CIR = simulate(anchor(x_a, y_a), tag(x_t, y_t))$
    $pk[:] \leftarrow findPeaks(CIR)$
    $totalPeaks \leftarrow length(peak)$
    $score \leftarrow 0$
    if $totalPeaks$ is 4 **then**
      $score \leftarrow totalPeaks \times$
      $\sqrt{(pk(4) - pk(3))^2 + (pk(3) - pk(2))^2 + (pk(2) - pk(1))^2}$
    else if $totalPeaks$ is 3 **then**
      $score \leftarrow totalPeaks \times$
      $\sqrt{(pk(3) - pk(2))^2 + (pk(2) - pk(1))^2}$
    else if $totalPeaks$ is 2 **then**
      $score \leftarrow totalPeaks \times \sqrt{(pk(2) - pk(1))^2}$
    else
      $score \leftarrow 0$
    end if
    $totalScore(x_a, y_a) \leftarrow totalScore(x_a, y_a) + score$
  end for
end for

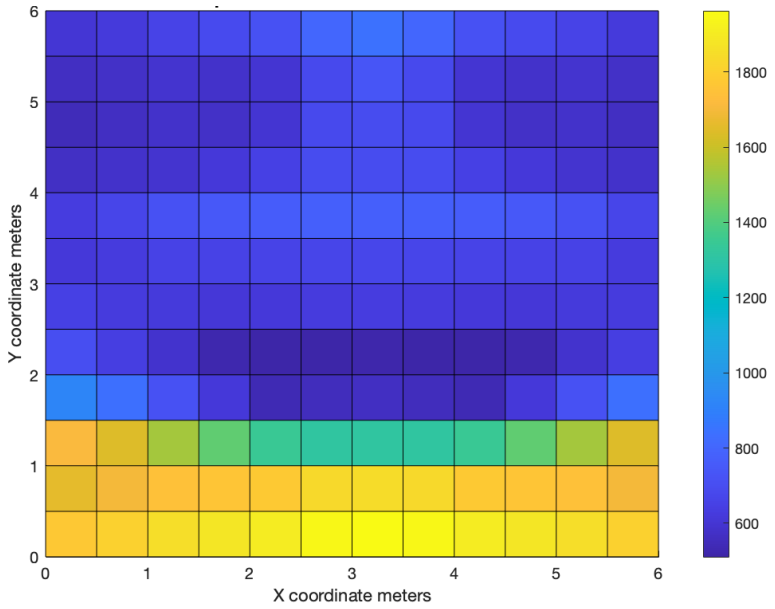

Figure 4.15: **Score calculation for different locations of the anchor.**

Chapter 5

Testbed Evaluation

This section present the testbed evaluation of the proposed methods. The results obtained with a single Multipath Component (reflective wall) present in the test environment are discussed first, followed by experiments involving two MPCs and localization in 3D space.

5.1 Localization with a Single MPC

In this evaluation, we utilize only one MPC, employing a single whiteboard. The evaluation board used is the Murata NXP SR150 Rev 3.3.

5.1.1 Experiment Setup

The experimental room setup is shown in Figure 5.1. The room's height, where the experiment takes place, is approximately 2.68 meters, while the tripod stands supporting the UWB sensor with a height of 1.06 meters. The blue markings in the figure represent distinct positions of the tag, each separated by approximately 1 meter, and these positions are measured using a measuring tape. The red line signifies the whiteboard employed to induce reflections in the experiment. The green point at the bottom of the figure denotes the anchor's position, comprising two PCB antennas spaced 1.6 cm apart, utilized for measuring the CIR.

5.1.2 Data Collection

Data collection was carried out using two Murata UWB boards, each equipped with an NXP microcontroller QN9090 and NXP SR150 UWB transreceiver. Upon powering up, one of the boards operates in controller mode (tag), while the other operates in controllee mode (anchor). The boards were configured to operate on channel 9 with a working frequency of 8 GHz.

5.1.3 Data Processing

When examining the CIRs from the collected data, additional reflections were identified. These reflections were presumed to originate from surfaces such as the ceiling and ground. This observation aligns with the findings reported by

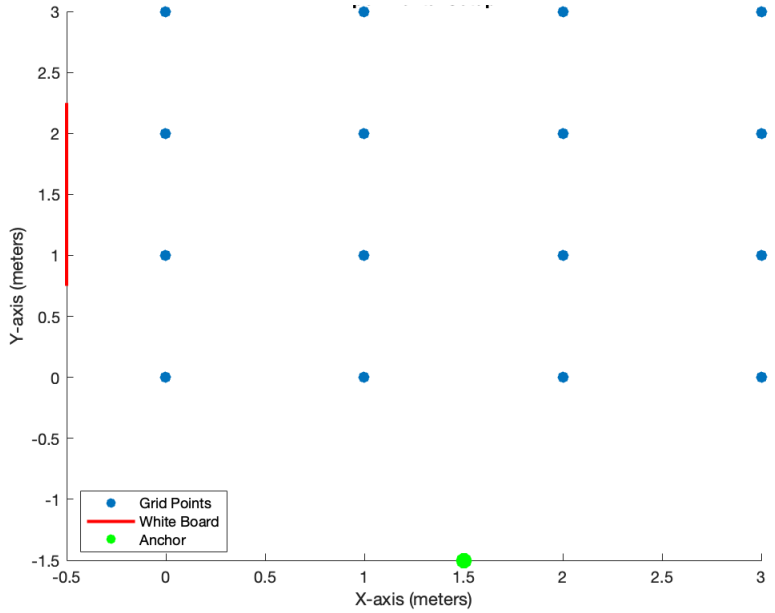

Figure 5.1: **Experimental settings of the anchor and tag positions.**

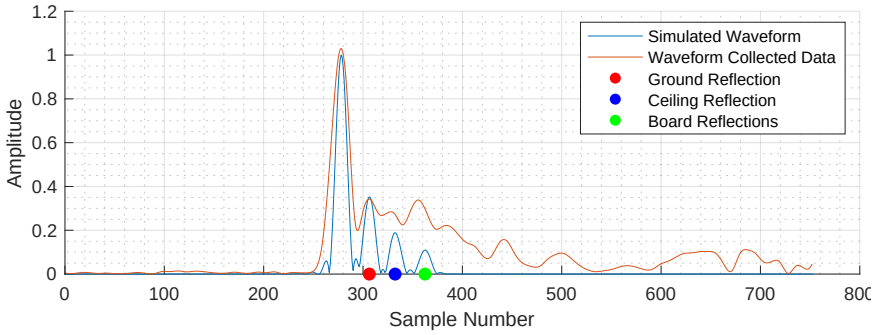

Figure 5.2: **Ideal representation of the received CIR.**

the authors of [13]. They also detected the presence of reflections from the ceiling, which supports our findings. Consequently, simulations were conducted to generate CIRs, incorporating information about the whiteboard, ceiling, and ground as surfaces for reflections. Subsequently, the waveform of the collected data was shifted to align the LOS index with that of the simulated waveform CIR. This adjustment allowed for a meaningful comparison between the two waveforms from the collected and simulated data as shown in Figure 5.2.

In Figure 5.2, the peaks are distinctly distributed, facilitating the clear identification of ground, ceiling, and whiteboard reflections. In Figure 5.4, the ground and ceiling reflections are not visibly apparent. The unpredictable nature of the ground and ceiling reflections may be attributed to the radiation pattern of the utilized antenna, as it could influence the behavior of these reflections. However, in Figure 5.5, the ground reflection merges with the whiteboard reflection, notably observed when the tag is positioned at coordinates (3,3). This mer-

Figure 5.3: **Indoor experimental setting of the anchor and the tag.**

ging occurs due to the lengthened path of the ceiling reflection, causing it to be observed after the whiteboard reflection.

We employ the likelihood method to estimate the positions of the tag as it difficult to distinguish the peaks of the white board from that of the ceiling and ground. We need only the virtual anchor information as this method does not require the peaks of the CIRs.

5.1.4 Results of Likelihood Method

We use the likelihood method to obtain the approximate location of the tag. Table 5.1 shows the results that are obtained. The cells in red signify error

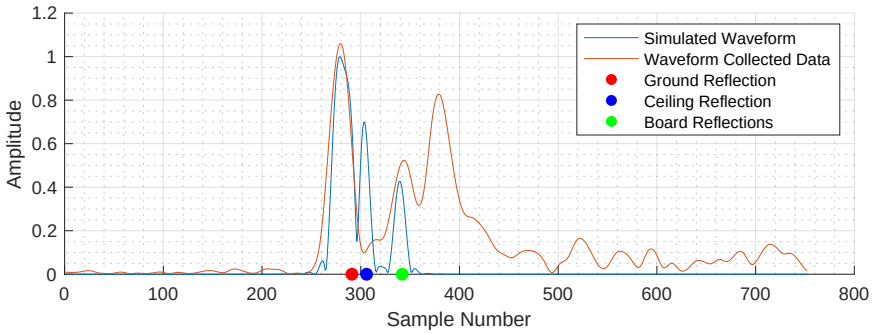

Figure 5.4: **Plot of a scenario when the ceiling and ground reflections are not visible in the CIR.**

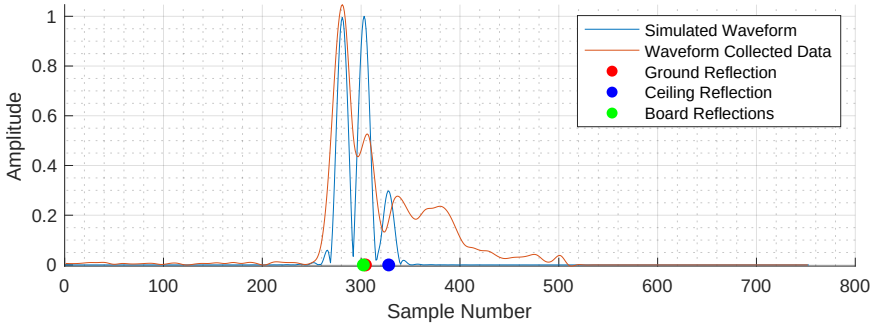

Figure 5.5: **Plot of CIR when ground reflection merges with the board reflection.**

Table 5.1: **Results for localization of tag in the experimental setup. The error of the results are displayed for the CIR that were obtained from individual antennas.**

Tag Location	**Antenna Error (m)**							
	Y : 0		**Y : 1**		**Y : 2**		**Y : 3**	
X	**1**	**2**	**1**	**2**	**1**	**2**	**1**	**2**
0	0.396	0.315	0.55	0.43	0.12	0.07	2.15	0.23
1	0.18	1.7	0.27	0.167	0.37	0.16	0.43	0.43
2	1.9	1.19	1.73	0.8	0.56	0.86	1.8	0.53
3	2.4	1.6	2.19	0.19	2.3	1.9	3.2	0.165

greater than 1 meter and cells in green colour signify error less than 1 meter.

In Figure 5.6, the approximated locations using the Likelihood method are depicted. Notably, tag locations with x coordinates less than 1.5 are detected relatively accurately, whereas positions with x coordinates greater than 1.5 exhibit larger errors. This discrepancy may be attributed to the proximity of points on the left side of the anchor to the white board, resulting in significantly higher amplitude of peaks due to the MPC.

5.1.5 Discussions

Challenges in the current data collection. The data collection in this evaluation is confronted with the following challenges:

1. **Potential Ground and Ceiling Reflections:** The data collected is susceptible to ground and ceiling reflections, introducing unwanted signals that may compromise the accuracy and reliability of the results.

2. **Convergence Issues between Ceiling/Ground and MPCs (White Board):** Ceiling/ Ground reflections sometimes get converged with the reflections of the whiteboard.

3. **Potential Additional Reflections Captured by the Receiver:** The receiver may inadvertently capture reflections beyond the intended signals, potentially introducing noise or interfering with the primary data.

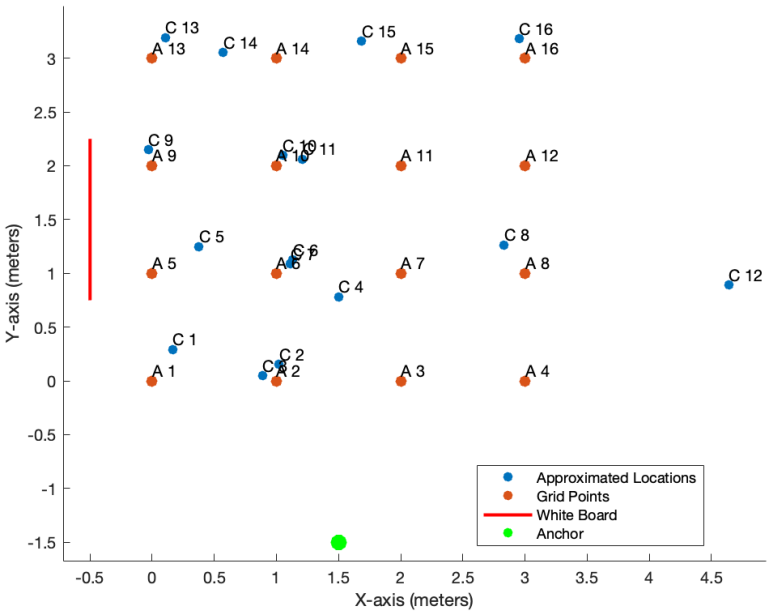

Figure 5.6: **Results obtained for calculated locations from the CIR acquired from Antenna two.**

4. **Difference in CIR:** When examining the CIRs from the two antennas, it was observed that the peak indexes differed significantly. This discrepancy led to substantial variations in the approximated locations of the tag based on the CIRs from each antenna. Additionally, the AoA derived from phase angles could not be accurately calculated due to these inconsistencies.

Potential solutions. The following suggestions outline improvements that could enhance localization from the collected data:

- A larger whiteboard or reflective surface could be utilized, as some points on the grid might not reflect from the current board's surface. This adjustment would potentially improve the coverage and accuracy.

- It is not known whether the surface of the white board is reflective, currently we are assuming that there is a reflective metal layer on the white board. Maybe an additional reflective layer could be added on to the surface of the white board to make sure that reflections take place.

- Adjusting the height of the tripod stand to align it more closely with both the ceiling and the ground. This alignment will ensure that reflections from the ceiling and ground consistently converge, leading to a heightened accuracy in identifying peaks. By achieving this convergence, the peaks could be more effectively distinguished, facilitating an improved identification process.

5.2 Localization with Two MPCs

In this section, we present the experiment that was carried out with two MPCs to counteract the problems that were faced when using a single MPC setup. This testing makes use of the newer revision of the UWB board Murata NXP Rev 4.1.

Enhancements with the New Board

With newer board there were some improvements that we observed when upgrading from the Rev 3.3 version of the board to Rev 4.1.

1. In the previous revision of the we observed that for antenna 2 in the CIR at larger indexes the amplitude drops to constant zero where as this was not the case for antenna 1's CIR. With the newer revision of the board this issue seems to be solved as it is no longer observed.

2. In the previous version of the board there were large differences observed in the CIR of the two antennas. As the antennas are placed 1.6 cms apart the CIR on the anchor should be similar. In the newer board the CIRs look quite similar with peaks occurring at almost the same indexes.

3. In the previous iteration of the board, when employing phase angles from the two CIRs to calculate AoA, faulty angles were observed. However, this issue appears to have been resolved with the revision of the board.

5.2.1 Experimental Setup

Following the results obtained in the preceding section, further experimentation was conducted involving the integration of an additional MPC into the setup. This round of testing also included longer MPCs that extended across the entire length of the area under consideration. Additionally, adjustments were made regarding the placement of the anchor/tag height, positioning it equidistant from both the ceiling and the ground. This modification aimed to reduce the occurrence of unwanted peaks in the CIR generated at the anchor.

The tag was positioned at a height similar to that of the anchor, ensuring comparable placements. In Figure 5.8, the various tag positions are denoted by blue circles. Based on our simulations, the optimal anchor location was determined to be at point $(2.5, 0)$, maintaining equidistance from both MPCs. However, this configuration promotes symmetry in the generated CIRs. For instance, if the tag were placed at points 6 and 7 in Figure 5.8, the resulting CIR's peak indexes at the anchor would be very similar. Therefore, in this experimental setup, the anchor was deliberately positioned 2 meters from MPC1 and 3 meters from MPC2 to remove the symmetry.

In Figure 5.9 we see the layout of the experiment described in the previous section with only 1 MPC. The difference now is that there are 2 MPC's instead of one and that the anchor is positioned in the middle, between the two MPC's. The results that we obtain after using the likelihood method can be seen that for various positions the locations are switched. For example, the approximated locations of 2 & 3 are switched. This phenomenon is even observed for locations

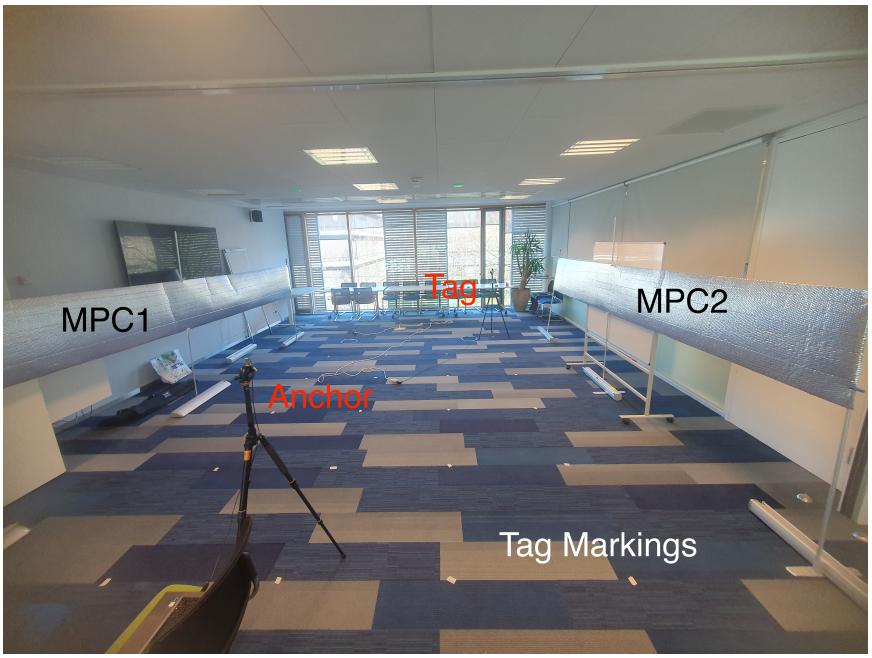

Figure 5.7: **Experimental setting of anchor and tag with two MPCs.**

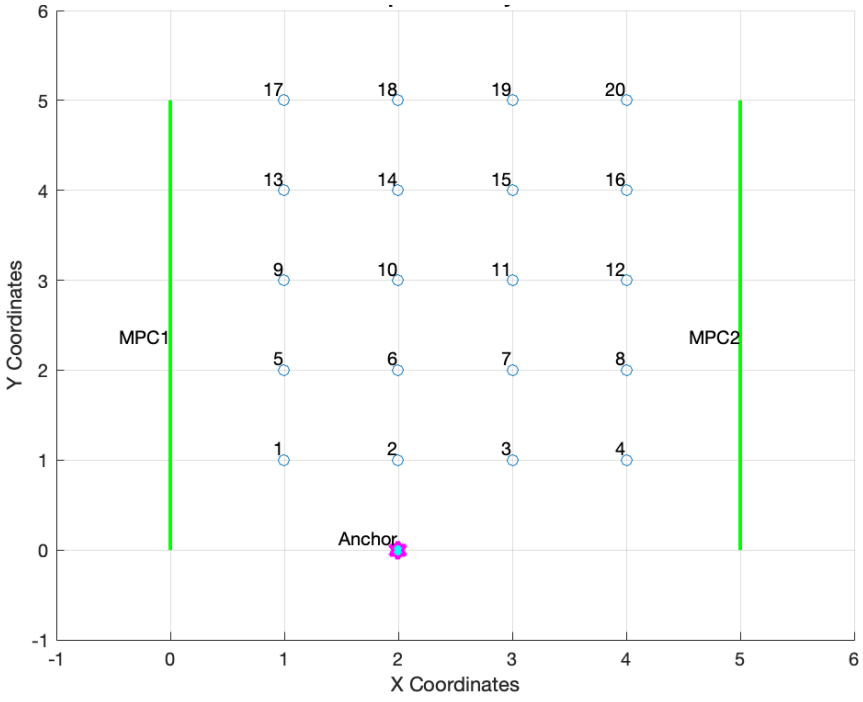

Figure 5.8: **Experimental settings of anchor and tag positions with two MPCs.**

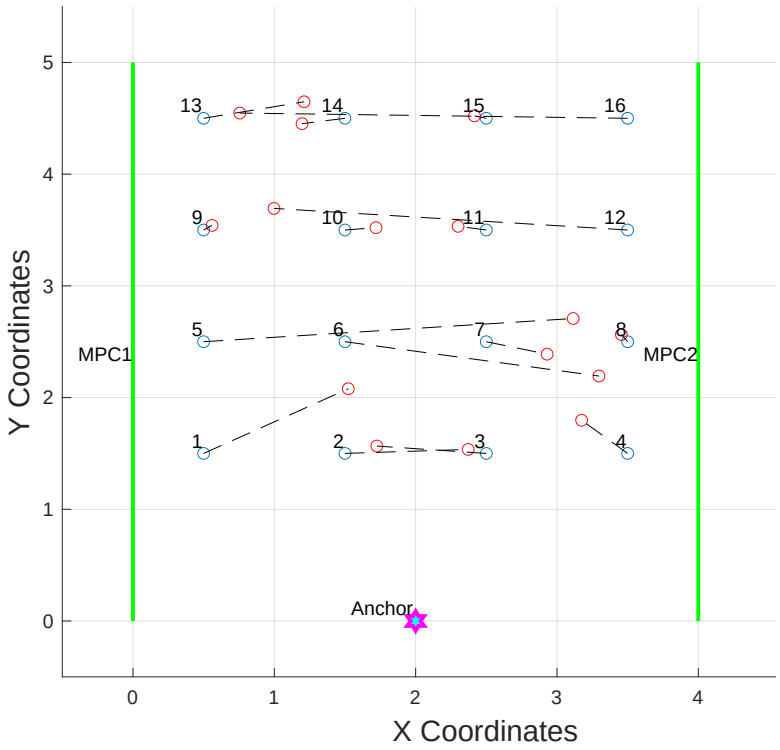

Figure 5.9: **Results with placing the anchor between the 2 MPCs.**

5, 12 and 16. Placing the anchor in between the two MPCs produces symmetry therefore it is not a good idea to do so.

Examining the Channel Impulse Responses (CIR)

Despite implementing precautions from the learnings in the previous round of testing, additional peaks in the CIR persist beyond those originating from the ground/ceiling and MPCs. Identifying the sources of these reflections proves challenging. Consequently, an alternative approach was adopted wherein we estimate which peaks in the CIR correspond to reflections from MPCs and the ceiling/ground.

CIRs are obtained from the two antennas on the chipset used, and the phase angle of the LOS signal is utilized to calculate the PDoA, as depicted in Figure 5.10. Peak pairs can be observed in the figure, they are usually peaks from the two CIR's having close by indexes usually within one or two samples (1-2 nanoseconds). Subsequently, Equation (5.1) is used to approximate the angle subtended by the tag with respect to the anchor (also known as the AoA). The c is speed of light, f is the frequency of the signal , l is the spacing between the antennas and $\Delta\phi$ is the phase difference obtained from the CIRs. The resulting location is labeled as Initial in Table 5.2.

$$\alpha = \arcsin \frac{\Delta\phi c}{2\pi l f}. \tag{5.1}$$

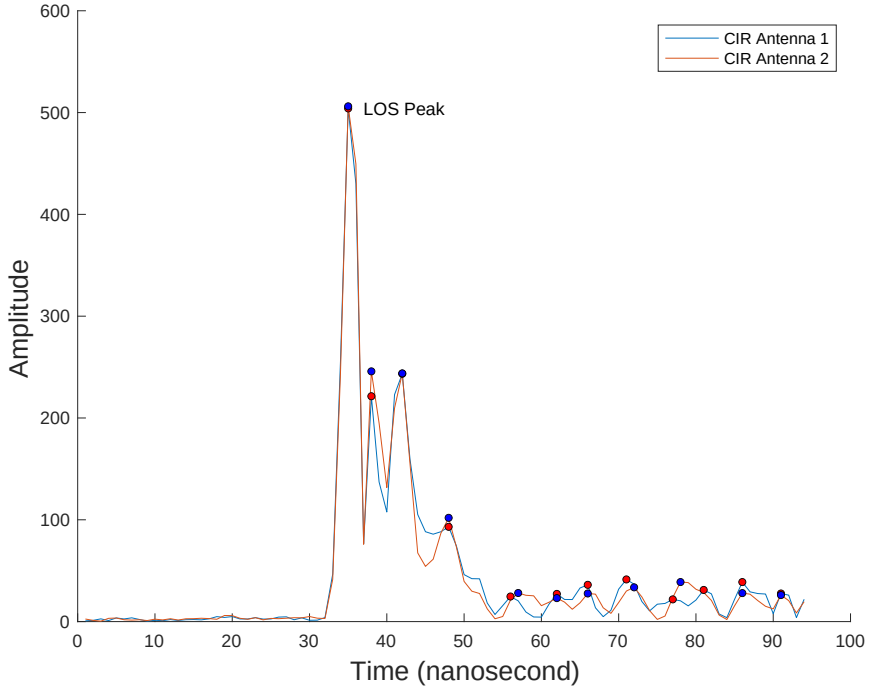

Figure 5.10: **Plot of amplitude of CIRs obtained from the two antennas of the UWB anchor.**

This method aids in estimating the tag's approximate location relative to the anchor. Subsequently, with this approximate location, we simulate the signal as if the tag were actually positioned at that particular spot. By analyzing this simulated signal, we can approximate the indices of the peaks originating from the MPCs and the ceiling/ground, as shown in Figure 5.11. We then select the peak index of the collected data that is closest to the peak index of the simulated waveform.

Given that the sensor provides the distance between the tag and the anchor, we leverage this data to compute the distance traveled by the signal reflected off the MPC. Initially, the distance returned by the sensor exhibited an error of approximately 30 cm DC offset. To compensate for this, a test was conducted wherein data was collected while maintaining varying distances between the tag and anchor. By comparing the ground truth distances with those measured by the sensor, the DC offset was calculated.

In Figure 5.11 we see that the second board reflection represented by the green marker would have been difficult to estimate but using the simulated data we can estimate the index of the MPC peak.

Distances covered by reflections from MPC can be estimated as follows:

$$D_{\mathbf{MPC}} = D_{\mathrm{LOS}} + \frac{(I_{\mathrm{MPC}} - I_{\mathrm{LOS}}) * c}{f}. \tag{5.2}$$

In the above formula, f represents the sampling frequency, c denotes the speed of light, and I stands for the index of the peak. The data was initially sampled

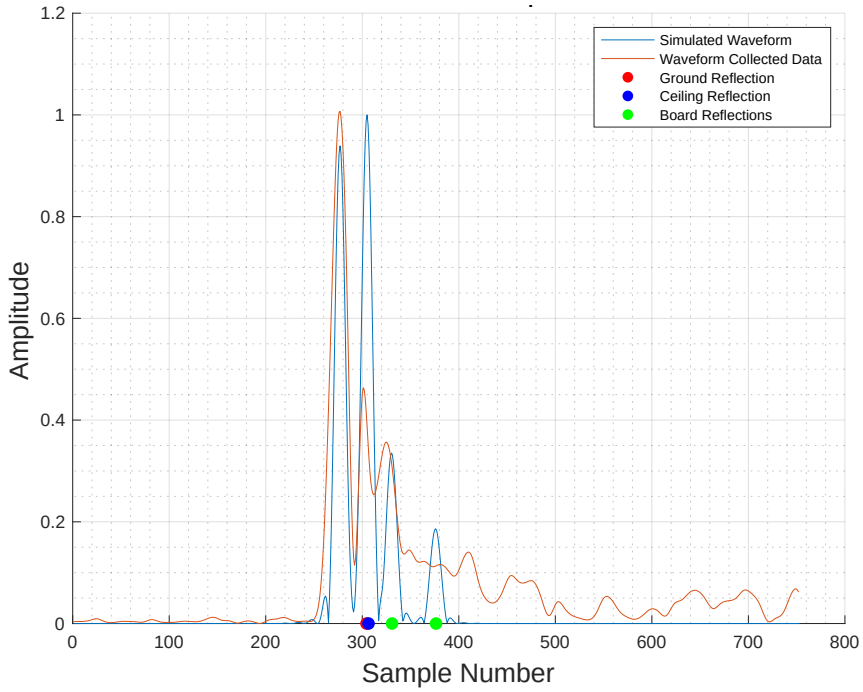

Figure 5.11: **Comparison of the collected data CIR and simulated CIR waveform showing the additional peaks near the MPC peaks.**

at a frequency of 1 GHz, but for a more precise estimation, we interpolated and upsampled the data to 8 GHz.

After estimating the distances covered by the MPC reflections, we employ the trilateration and f-min search methods to estimate the position of the tag. The outcomes from this process are labeled as Iteration 1.

Subsequently, the results obtained from Iteration 2 involve repeating these steps for another iteration. The outcomes obtained from this iteration are labeled Iteration 2, as shown in Table 5.2.

Angle estimation of MPC signals using PDoA

By analyzing the CIRs captured by the two antennas, we pinpoint the peak indexes and compute the phase angles at those specific indexes for the MPCs. Subsequently, using the phase angles obtained from both antennas, we calculate the PDoA for the MPCs. We observed that for locations close to the MPCs (1, 5, 9, 13, 17, 4, 8, 12, 16 and 20), the angles of the reflected signals were relatively accurate, with errors typically falling within the range of 2-5 degrees. Despite this promising accuracy, attempts to localize the tag using these angles resulted in significant errors.

Visualising the IQ plot of CIR

We tried to visualize the real and imaginary parts of the CIR for all the locations in the collected data. Figure 5.12 illustrates the IQ plot for location 12.

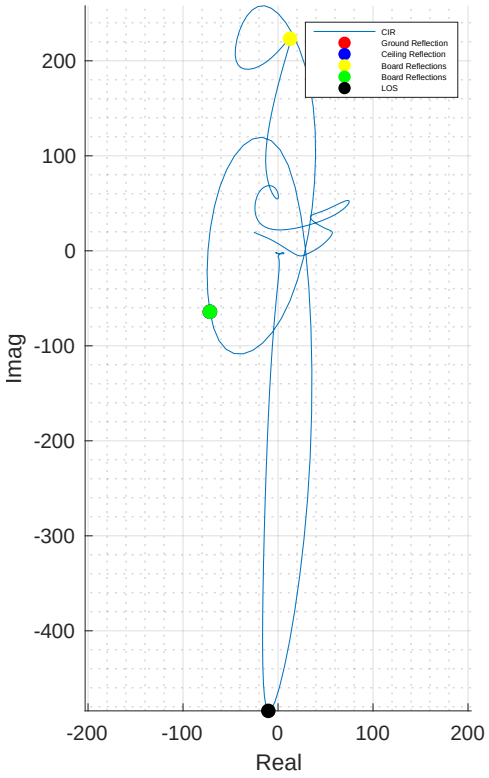

Figure 5.12: **Plot of complex CIR of collected data showing that for certain location locations localization can be improved by aligning the peak index at sharp turns in the loop in the IQ plot.**

In this plot, the black marker represents the LOS, the yellow marker signifies reflection of MPC 1, and the green marker denotes reflection from MPC 2. We observed that when peaks occur for reflections from different MPCs, they form loops similar to the one depicted by the black and yellow markers in the figure. Notably, the green marker does not fall on the extreme end of the loop. However, shifting its position to align directly at the end of the loop has shown to reduce error in localizing the tag. This leads to aligning the peak index of the reflection from MPC to be adjusted. Similar observations were made for tag locations 10 and 14 as well.

5.2.2 Performance Evaluation

In the following section, the performance evaluation for localization using three methods is discussed. First, the fminsearch method is examined, followed by the trilateration method, and finally, the likelihood method.

Performance Evaluation of the Fminsearch Method

The results that are obtained using the fminsearch method are shown in Table 5.2. The Initial results are the locations approximated using distance data and

Table 5.2: **Results for localization of tag in the experimental setup with two MPCs for the fminsearch method. The error of the results are displayed for the CIR that were obtained from individual antennas.**

Errors (centimeters)					
		Iteration 1		Iteration 2	
Location	**Intial**	**Antenna 1**	**Antenna 2**	**Antenna 1**	**Antenna 2**
1	9.31	13.82	1.61	31.1	1.24
2	2.59	29	32	16	15
3	15.97	20.2	20.2	5.93	5.93
4	0	0	0	0	0
5	5.55	42.13	42.13	30.89	30.89
6	3.06	30.35	30.35	66.1	66.1
7	14.72	5.83	46.88	2.94	68.85
8	25.03	16.3	12	17	11.64
9	6.45	15.85	10.36	51.79	28
10	3.25	15.6	2.9	19.05	1.1
11	9.73	111	35.2	73	17.69
12	23.3	41	3.85	66	3.6
13	1.88	15.62	4.98	9.54	3.88
14	2.89	25.97	25.3	24.9	8.79
15	13.13	33.02	14.5	14.79	8.59
16	15.9	10.18	1.99	41	16.99
17	9.09	48	32	66	25
18	2.61	8	72.65	97	98
19	23.69	14.49	14.9	7.04	7.04
20	15.8	0.74	10.69	8	22.83
AVG	10.1975	24.855	20.7245	32.4035	22.058

angle calculated using phase angles from the two CIRs. The Iteration 1 of the results are the locations estimated using the fminsearch method. The results which are highlighted in green denote that the results for them were better than that of Initial results.

For Iteration 1 we select the results from Antenna 2 as they provide better results. In general, the outcomes labeled as Initial tend to outperform those of Iteration 1 (Antenna 2). However, for locations close to MPC1 and MPC2, Iteration 1 offers better results. This discrepancy arises from the accuracy of the angle estimated from the phase angles of Line-of-Sight (LOS) peaks in both CIRs, which are used to calculate the AoA using Equation (5.1). Specifically, when the angle subtended by the tag in relation to the anchor is low, the estimated error remains minimal. However, as the angle increases, the error starts to escalate. This phenomenon is attributed to the decreasing radiation pattern of the antenna for steeper angles. Consequently, locations near the MPCs exhibit steeper angles, resulting in higher Initial location estimation errors. Nonetheless, through Iteration 1, the localization accuracy is increased at points closer to MPC's.

The results obtained from Iteration 2 exhibit higher error rates. This arises from the fact that in this method, we estimate the position of the tag using reflection information from the MPC that is further away. Additionally, the

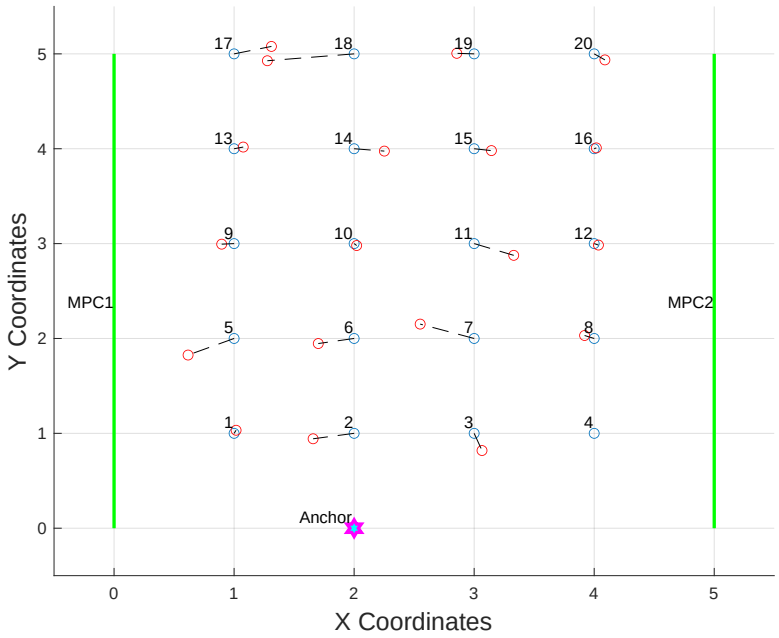

Figure 5.13: **Results of the fminseach method with two MPCs.**

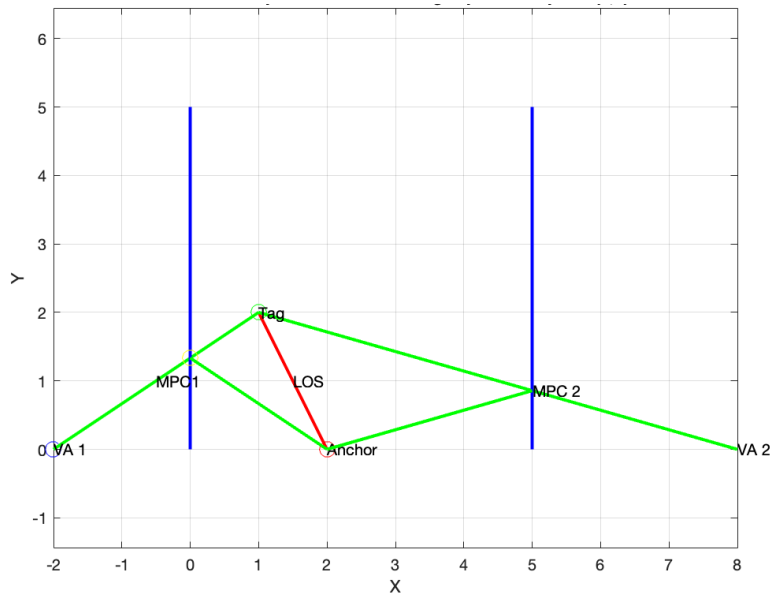

Figure 5.14: **Paths covered by signals coming from different anchors.**

index of the MPC peak, which is further away, typically entails a certain margin of error, contributing to the overall higher error rates observed in Iteration 2 when compared with Iteration 1.

In Figure 5.13 we can see the results are quite accurate for locations close to the MPCs except location 5. This shows that the reflection peak index are

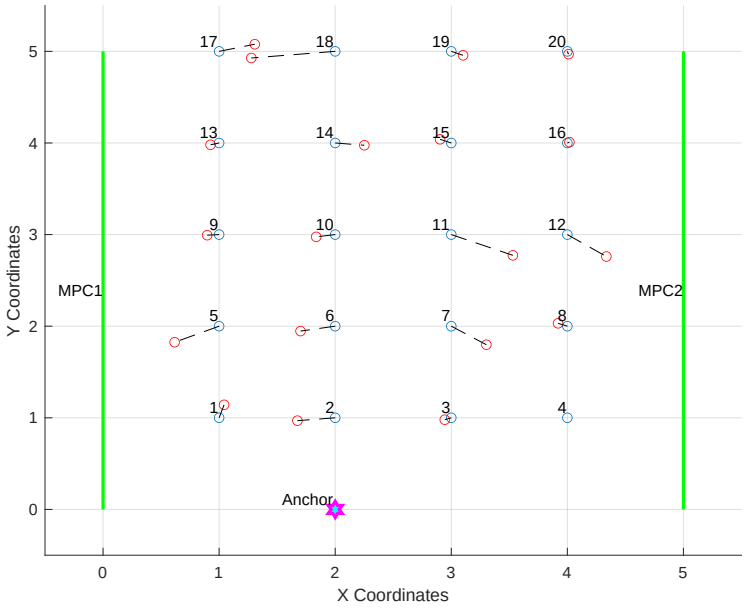

Figure 5.15: **Results of the Trilateration method with two MPCs.**

more accurate for locations close to the MPCs which leads to better location accuracy. As the distance of tags increases from the MPCs the accuracy of the tags drops. In Figure 5.14 we see the different paths that are taken by the LOS and MPC's. It can be seen that signal reflecting of MPC2 has to cover a much larger distance when compared to the distance that is covered by signals from LOS and MPC1.

Performance Evaluation of the Trilateration Method

The results obtained through the trilateration method are depicted in Figure 5.15. We employed the same analysis technique outlined in Section 5.2.1, as the fminsearch method also relies on peak indexes in the CIR. On average, an error of approximately 24.24 centimeters was observed. Notably, for localization with this method, data from antenna two was primarily utilized, as it gave better results, as mentioned in Section 5.2.1.

Performance Evaluation of the Likelihood Method

When using the likelihood method to estimate the tag's possible location, significant discrepancies were noted for certain positions. This discrepancy arises from additional peaks observed in the CIR data, primarily caused by reflections from the ceiling and ground surfaces. These reflections exert a substantial influence on the accuracy of location approximation using this method.

The results obtained using this method are shown in Figure 5.16. Notably, locations such as 3, 6, 12, and 14 exhibit notably high errors in approximation. To investigate the underlying cause, we examined the CIR for location 15. It was observed that a dominant peak corresponding to the ceiling and ground reflections significantly influenced the waveform, as shown by the blue waveform

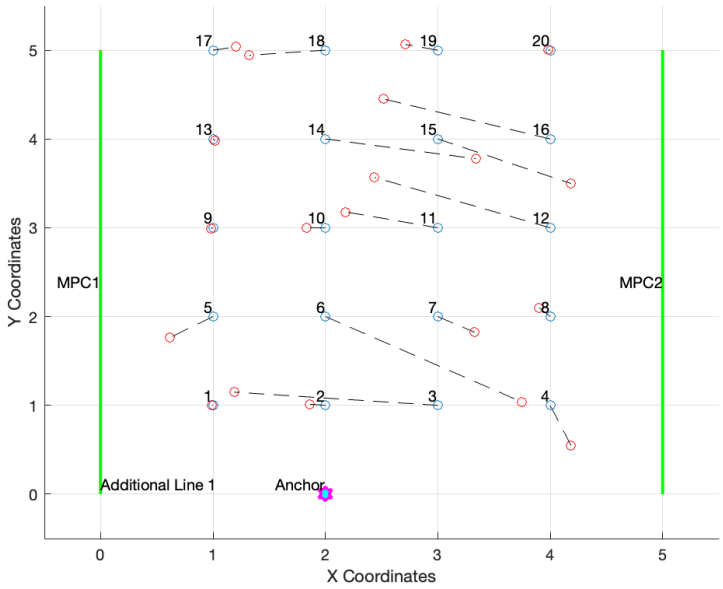

Figure 5.16: **Results of the Likelihood method with two MPCs before removal of ceiling and ground reflections from the CIR.**

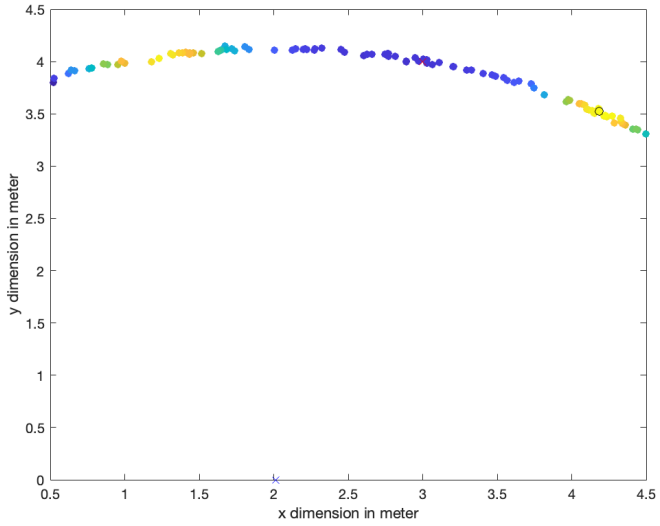

Figure 5.17: **Sample points with the likelihood method at Location 15.**

in Figure 5.18. This dominant peak led to the erroneous approximation of the tag's location. The likelihood of the different sample points for location 15 can be observed in Figure 5.17. The yellow regions in the figure signifies higher likelihood and regions in dark blue signify regions of lower likelihood. The red cross at location (3,4) shows the actual location of the tag. And black circle at location (4,3.5) shows the approximated location due to it having the highest

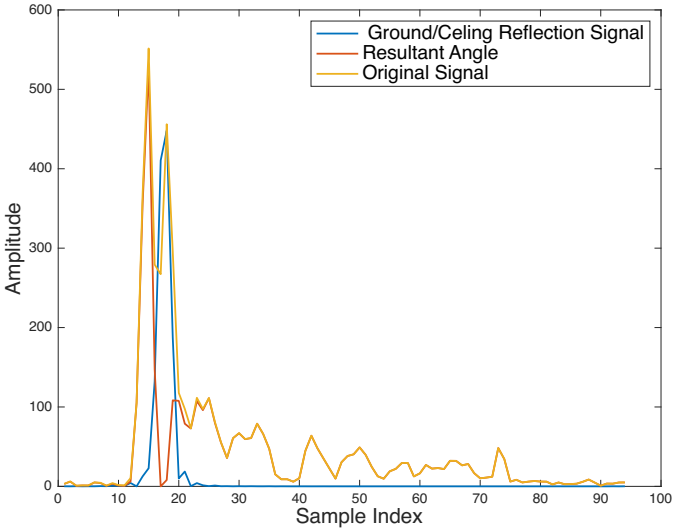

Figure 5.18: **Waveforms of CIR at location 15 with the removal of ceiling/ground reflection.**

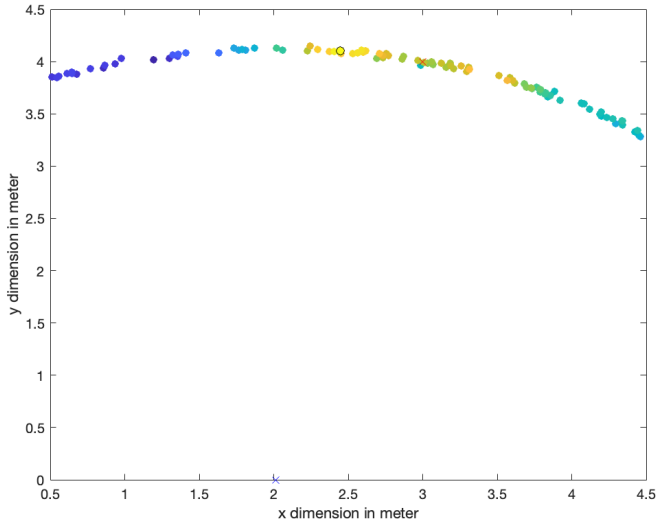

Figure 5.19: **Sample points with the likelihood method at Location 15 after removing the reflections from ceiling ground.**

likelihood score. In Figure 5.18 we see three different waveforms. The yellow line shows the original waveform that is received at the anchor. The blue line is the approximation of the ceiling/ground reflection. We then try to subtract the ceiling/ground signal (blue signal) from the signal that is received at the anchor (yellow, original signal). The resultant that is obtained is shown with an orange line in Figure 5.18.

The likelihood of the sample points at location 15 can then be seen in Figure

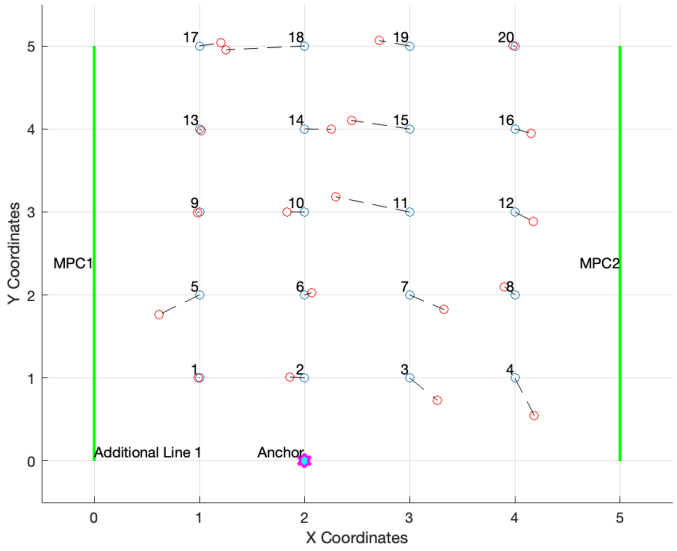

Figure 5.20: **Results of the Likelihood method with two MPCs after removal of the ceiling and ground reflection from the CIR.**

5.19. Similarly we try to implement the removal of ceiling/ ground reflection at multiple locations and try to localize the tag using the likelihood method. This process is done to remove the additional peaks in the CIR. The results that are obtained after removal of these additional peaks can be seen in Figure 5.20. Using this method we get an average error of 26 centimeters across the 20 locations to localize the tag.

Comparison of Results

In Figure 5.21, the results of the three localization methods are presented. The fminsearch method demonstrates the best performance, followed by the algebraic and likelihood methods. The fminsearch and algebraic methods both achieve errors of less than 42 centimeters for 90% of the locations. The likelihood method achieves errors of less than 56 centimeters for 90% of the locations. Notably, the likelihood method only requires data from one antenna, whereas the fminsearch and algebraic methods necessitate data from two antennas to accurately identify the reflections peaks within the CIR from the MPCs. However, the likelihood method's data required cleaning to remove ceiling and ground reflections, as these dominant peaks adversely affected localization accuracy.

5.3 3D Localization

After localising the tag in a 2D plane we even wanted to explore the possibility of localising the tag in a 3D space and it is possible to do so for certain locations because of the ceiling and ground reflections that we get in CIR that is received on the anchor. When we vary the height of the tag while keeping the height of the anchor consistent, we can utilize the peak indexes estimated from the CIR to obtain a rough estimate of the tag's position in 3D space, particularly

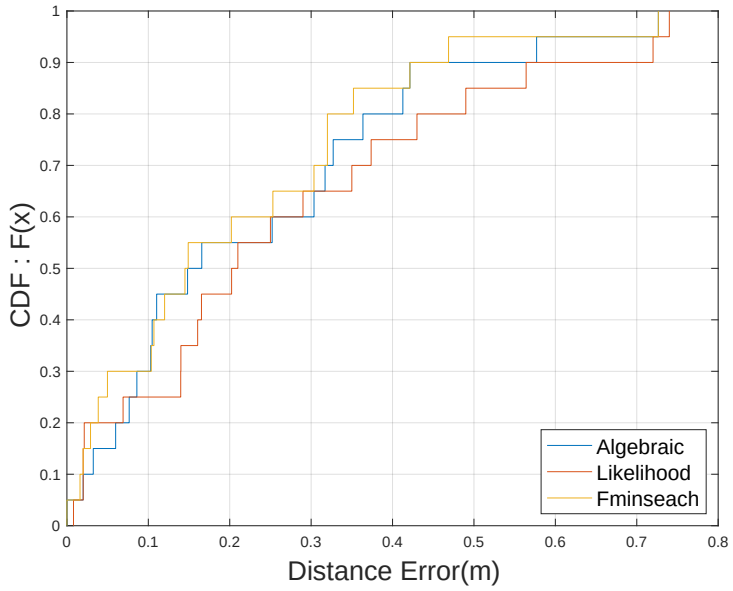

Figure 5.21: **CDF results of the three methods used for localization.**

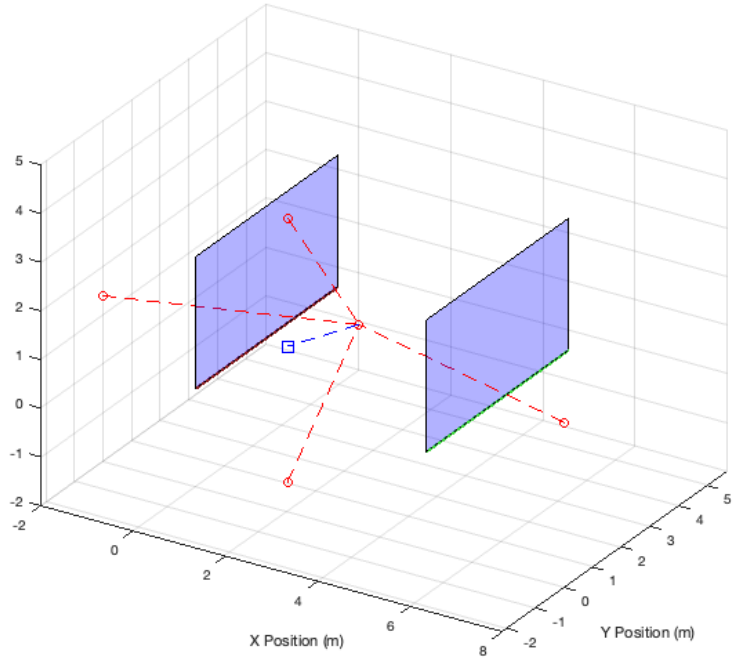

Figure 5.22: **Path traversed by signals from VAs in 3D localization.**

if the peaks do not converge. As depicted in Figure 5.22, two additional VA's are introduced because the ceiling and ground surfaces are now considered as MPCs apart. We leverage this information to calculate the height of the tag. The MPCs present on the left and right sides of the anchor are then used to localize the tag in 2D space.

Table 5.3: **Results of the 3D Localization.**

Location	Coordinates (m)			Height Error (cm)	3D Error (cm)
	X	Y	Z		
1	2	2.5	0.8	6	8
2	2	2.5	1.05	4	13
3	2	2.5	1.38	12	19
4	2	2	1.05	18	26
5	2	2	0.795	0.109	21

In Figure 5.22, the blue square represents the position of the anchor, while the red dots depict the VA's and the tag. It's observed that the signal traverses through five different anchor/VA's. In this specific scenario, the anchor was positioned at a height of 1.3 meters, and the tag was placed at a height of 0.8 meters with coordinates (2, 2.5). For accurate localization of the tag in 3D space, the distances covered by the signals from different anchors need to be varying. If the distances are similar, convergence may occur, leading to erroneous estimations of the tag position. At this particular location, five distinct peaks are observed. By utilizing the peak indexes, we calculate the distances and employ the fminsearch or algebraic method to localize the tag. We get an error of approximately 8 cm when trying to localise the tag at this particular location. The error was mainly along the height which was approximated to 0.72 meters.

In another test conducted at the same location of the tag and anchor, we varied the height of the tag by increasing it to 1.05 meters and collected the data. The error this time was found to be around 13 cm and the height was approximated to be around 1.01 meters. When attempting to scale this experiment to a larger setting, we encountered challenges due to the convergence of peaks resulting from reflections from different MPCs. This convergence posed difficulties in reliably interpreting the results. This led to fewer peaks being detected, hindering our ability to draw meaningful conclusions.

Table 5.3 shows the results that we obtained for certain locations where we were able to obtain distinct peaks for the different MPC's in the CIR and subsequently able to localize the tag. This method of 3D localization might be more effective in environments where the height of the room is much larger. As the larger height will enable peaks corresponding to the different MPC's to be distinctly visible.

Chapter 6

Conclusions

The research in this report is aimed at understanding the effects of multipath signals that are encountered in UWB communications and if it can be utilized to enhance the localization accuracy of tags with the extra information that can be captured and visualized in the CIR. Generally multiple anchors are utilized to localize tags but in this investigation we try to localize the tag using a single anchor and create multiple VAs with the help of MPCs. In the research that was conducted there were several methods identified namely the Likelihood, Algebraic and fminsearch methods. Simulations were conducted with these methods by creating environments with anchor & tags along with MPCs the reflective surfaces on which the signals reflect. After obtaining results with the simulations which showed that the three methods are effective for localization along with some minor drawbacks.

After it was proven in simulations that localizing the tags using these methods along with the reflection data is possible, we started with the experiments. Data was collected using NXP's SR 150 UWB tags which consisted of two antennas so that CIR could be collected on these two separate antennas which are separated by a certain distance. An experimental environment was created in an indoor space which consisted of two MPCs along with a fixed position of the anchor carefully decided keeping mind positions of the MPCs. The tag was subsequently placed at several locations in the indoor space and data was collected at each point. After the data was collected different methods were used to find the location of the tag.

It was observed in the CIR of the collected data that there existed several extra reflections along with the reflections that came from MPCs. Reflection that we consistently observed were the ceiling and ground reflections. These reflections at many points even caused convergence of peaks in the CIR along with the reflections coming from the different MPCs. Several ideas were implemented then to localize the tag to improve the accuracy of localizing the tag in the noisy data that was obtained along with reflections from unknown sources. For the likelihood method we adopted the implementation of cleaning the data by removal of unwanted peaks from the CIR. And in fminsearch and algebraic methods by ignoring the extra peaks by making use of two antennas present on the board to calculate the approximate AoA to get an idea where the possible indexes of reflection peaks from MPC peaks existed.

In the final results it was observed that the likelihood method had localiz-

ation error of 26 cm on average over the different locations of the tag. The fminsearch method produced an error of 20.7 centimeters and the algebraic method obtained average accuracy of 24 centimeters. It can then be seen that the fminsearch method gives better results over the likelihood method in terms of accuracy. But the likelihood method just requires data from one antenna and subsequently just requires one CIR. Since the data we collected consisted of reflections from unknown sources we utilize the data from two antennas for the fminsearch and algebraic method. When seen in general the fminsearch method does not produce results better than the traditional method of AoA between the two devices. But it does produce better accuracy when the tags are positioned near MPCs. As the tag moves further away from the MPCs the accuracy obtained from methods making use of the reflection data goes down. But for locations near the MPCs this method is quite accurate and it can be used in applications and scenarios where AoA is quite large as the errors with the traditional methods goes down as the AoA crosses 60 degree angles.

6.1 Future Work

This research presents several opportunities for enhancements to increase localization accuracy and explore various applications.

6.1.1 Oversampling of CIR

The obtained CIRs were sampled at a frequency of 1 GHz and then oversampled by a factor of 8 using interpolation methods like spline. This interpolation might have introduced inaccuracies by approximating the CIR amplitude incorrectly. Future work could focus on using sensors with higher sampling rates, eliminating the need for significant oversampling. Higher sampling rates could improve the precision of peak positioning in the CIR and, consequently, enhance location estimation accuracy. As UWB sensors evolve with better sampling capabilities, utilizing reflection data embedded within the CIRs could further improve tag accuracy.

6.1.2 Selection of Reflective Materials for MPCs

Another area for potential improvement is the selection of reflective materials for MPCs. A systematic investigation into materials that exhibit minimal signal attenuation could optimize signal strength retention and enhance localization accuracy. Identifying the most effective materials for reflecting UWB signals could significantly improve the reliability and precision of localization systems.

6.1.3 Testing Across Diverse Indoor Environments

Future research could benefit from testing and collecting data in a variety of indoor environments with different ceiling heights and ground materials. This approach would help to observe and understand the impact of varying ground and ceiling reflections on localization accuracy. By analyzing how different environments affect signal behavior, more robust and adaptable localization algorithms

could be developed. This comprehensive testing could lead to insights on optimizing UWB localization systems for diverse real-world applications, enhancing their reliability and performance in various settings.

6.1.4 Applications

The approach of utilizing multipath signals has several promising applications:

Localization of Indoor Robots

This technique could be employed to localize robots in enclosed indoor spaces by leveraging reflective data. Accurate localization is crucial for efficient navigation and task execution in automated systems.

Localization of Bicycles in Crowded Parking Spaces

Another potential application is the localization of bicycles within crowded parking areas. This method could facilitate efficient bicycle retrieval, streamlining the process for users seeking their bicycles in densely packed environments.

Asset Tracking in Warehouses

The multipath signal approach can also be applied to track assets in large warehouses. By accurately localizing inventory items, this method can improve stock management, reduce search times, and enhance overall operational efficiency.

Smart Home Automation

In smart home environments, utilizing multipath signals for localization can enhance the functionality of automated systems. For example, precise localization of household items or individuals can improve the responsiveness of smart lighting, heating, and security systems, making home automation more efficient and user friendly.

Bibliography

[1] Mahnoor Anjum, Muhammad Abdullah Khan, Syed Ali Hassan, Aamir Mahmood, Hassaan Khaliq Qureshi, and Mikael Gidlund. Rssi fingerprinting-based localization using machine learning in lora networks. *IEEE Internet of Things Magazine*, 3(4):53–59, 2020.

[2] Damir Arbula and Sandi Ljubic. Indoor localization based on infrared angle of arrival sensor network. *Sensors*, 20(21):6278, 2020.

[3] Atul Bansal, Akshay Gadre, Vaibhav Singh, Anthony Rowe, Bob Iannucci, and Swarun Kumar. Owll: Accurate lora localization using the tv whitespaces. In *Proceedings of the 20th International Conference on Information Processing in Sensor Networks (co-located with CPS-IoT Week 2021)*, pages 148–162, 2021.

[4] Esmat Bekir. *Introduction to modern navigation systems*. World scientific, 2007.

[5] Jona Beysens, Qing Wang, Ander Galisteo, Domenico Giustiniano, and Sofie Pollin. A cell-free networking system with visible light. *IEEE/ACM Transactions on Networking*, 28(2):461–476, 2020.

[6] Joan Bordoy, Johannes Wendeberg, Christian Schindelhauer, and Leonhard M Reindl. Single transceiver device-free indoor localization using ultrasound body reflections and walls. In *2015 International Conference on Indoor Positioning and Indoor Navigation (IPIN)*, pages 1–7. IEEE, 2015.

[7] Lorenzo Capineri and Andrea Bulletti. Ultrasonic guided-waves sensors and integrated structural health monitoring systems for impact detection and localization: A review. *Sensors*, 21(9):2929, 2021.

[8] Matthias Cäsar, Tobias Pawelke, Jan Steffan, and Gabriel Terhorst. A survey on bluetooth low energy security and privacy. *Computer Networks*, 205:108712, 2022.

[9] Arthur Charléty, Mathieu Le Breton, Eric Larose, and Laurent Baillet. 2d phase-based rfid localization for on-site landslide monitoring. *Remote Sensing*, 14(15):3577, 2022.

[10] Rui Chen, Xiyuan Huang, Yan Zhou, Yilong Hui, and Nan Cheng. Uhf-rfid-based real-time vehicle localization in gps-less environments. *IEEE Transactions on Intelligent Transportation Systems*, 23(7):9286–9293, 2021.

[11] Zhenghua Chen, Qingchang Zhu, and Yeng Chai Soh. Smartphone inertial sensor-based indoor localization and tracking with ibeacon corrections. *IEEE Transactions on Industrial Informatics*, 12(4):1540–1549, 2016.

[12] Chia-Hsin Cheng and Siang-Jhih Syu. Improving area positioning in zigbee sensor networks using neural network algorithm. *Microsystem Technologies*, 27:1419–1428, 2021.

[13] M Cimdins, SO Schmidt, and H MAMPI Hellbrück. Multipath-assisted device-free localization with magnitude and phase information. In *Proceedings of the 2020 International Conference on Localization and GNSS (ICL-GNSS), Tampere, Finland*, pages 2–4, 2020.

[14] Amalia Lelia Crețu-Sîrcu, Henrik Schiøler, Jens Peter Cederholm, Ion Sîrcu, Allan Schjørring, Ignacio Rodriguez Larrad, Gilberto Berardinelli, and Ole Madsen. Evaluation and comparison of ultrasonic and uwb technology for indoor localization in an industrial environment. *Sensors*, 22(8):2927, 2022.

[15] Igor Dotlic, Andrew Connell, Hang Ma, Jeff Clancy, and Michael McLaughlin. Angle of arrival estimation using decawave dw1000 integrated circuits. In *2017 14th Workshop on Positioning, Navigation and Communications (WPNC)*, pages 1–6. IEEE, 2017.

[16] Hassoon Salman Fahama, Karim Ansari-Asl, Yousef Seifi Kavian, and Mehdi Naderi Soorki. An experimental comparison of rssi-based indoor localization techniques using zigbee technology. *IEEE Access*, 2023.

[17] Georg Fischer, Joan Bordoy, Dominik Jan Schott, Wenxin Xiong, Andrea Gabbrielli, Fabian Höflinger, Kai Fischer, Christian Schindelhauer, and Stefan Johann Rupitsch. Multimodal indoor localization: Fusion possibilities of ultrasonic and bluetooth low-energy data. *IEEE Sensors Journal*, 22(6):5857–5868, 2022.

[18] Giovanni Fusco and James M Coughlan. Indoor localization using computer vision and visual-inertial odometry. In *Computers Helping People with Special Needs: 16th International Conference, ICCHP 2018, Linz, Austria, July 11-13, 2018, Proceedings, Part II 16*, pages 86–93. Springer, 2018.

[19] Bernhard Großwindhager, Michael Rath, Josef Kulmer, Mustafa S Bakr, Carlo Alberto Boano, Klaus Witrisal, and Kay Römer. Salma: Uwb-based single-anchor localization system using multipath assistance. In *Proceedings of the 16th ACM Conference on Embedded Networked Sensor Systems*, pages 132–144, 2018.

[20] Weipeng Guan, Shihuan Chen, Shangsheng Wen, Zequn Tan, Hongzhan Song, and Wenyuan Hou. High-accuracy robot indoor localization scheme based on robot operating system using visible light positioning. *IEEE Photonics Journal*, 12(2):1–16, 2020.

[21] Zhang Han, Chen Mingxia, and Li Shunyan. Research on node location algorithm of zigbee based on optimized neural network. In *2020 International Conference on Computer Engineering and Application (ICCEA)*, pages 693–698. IEEE, 2020.

[22] Lifei Hao, Baoqi Huang, Bing Jia, and Guoqiang Mao. Dhcloc: A device-heterogeneity-tolerant and channel-adaptive passive wifi localization method based on dnn. *IEEE Internet of Things Journal*, 9(7):4863–4874, 2021.

[23] Milad Heydariaan, Hossein Dabirian, and Omprakash Gnawali. Anguloc: Concurrent angle of arrival estimation for indoor localization with uwb radios. In *2020 16th International Conference on Distributed Computing in Sensor Systems (DCOSS)*, pages 112–119. IEEE, 2020.

[24] Kyungki Kim, Sining Li, Milad Heydariaan, Nour Smaoui, Omprakash Gnawali, Wonho Suh, Min Jae Suh, and Jung In Kim. Feasibility of lora for smart home indoor localization. *Applied Sciences*, 11(1):415, 2021.

[25] Josef Kulmer, Stefan Hinteregger, Bernhard Grosswindhager, Michael Rath, Mustafa S Bakr, Erik Leitinger, and Klaus Witrisal. Using decawave uwb transceivers for high-accuracy multipath-assisted indoor positioning. In *2017 IEEE International Conference on Communications Workshops (ICC Workshops)*, pages 1239–1245. IEEE, 2017.

[26] Josef Kulmer, Erik Leitinger, Paul Meissner, Stefan Hinteregger, and Klaus Witrisal. Cooperative localization and tracking using multipath channel information. In *2016 International Conference on Localization and GNSS (ICL-GNSS)*, pages 1–6. IEEE, 2016.

[27] Jeffrey C Lagarias, James A Reeds, Margaret H Wright, and Paul E Wright. Convergence properties of the nelder–mead simplex method in low dimensions. *SIAM Journal on optimization*, 9(1):112–147, 1998.

[28] Antonio Lazaro, Marc Lazaro, and Ramon Villarino. Room-level localization system based on lora backscatters. *IEEE Access*, 9:16004–16018, 2021.

[29] Nicolas Le Dortz, Florian Gain, and Per Zetterberg. Wifi fingerprint indoor positioning system using probability distribution comparison. In *2012 IEEE international conference on acoustics, speech and signal processing (ICASSP)*, pages 2301–2304. IEEE, 2012.

[30] Peizheng Li, Han Cui, Aftab Khan, Usman Raza, Robert Piechocki, Angela Doufexi, and Tim Farnham. Deep transfer learning for wifi localization. In *2021 IEEE Radar Conference (RadarConf21)*, pages 1–5. IEEE, 2021.

[31] Junjie Liu and R Jain. Survey of wireless based indoor localization technologies. *Department of Science & Engineering, Washington University*, 2014.

[32] Andrea Motroni, Alice Buffi, and Paolo Nepa. A survey on indoor vehicle localization through rfid technology. *IEEE Access*, 9:17921–17942, 2021.

[33] Iynkaran Natgunanathan, Niroshinie Fernando, Seng W Loke, and Charitha Weerasuriya. Bluetooth low energy mesh: Applications, considerations and current state-of-the-art. *Sensors*, 23(4):1826, 2023.

[34] Abdelmoumen Norrdine. An algebraic solution to the multilateration problem. In *Proceedings of the 15th international conference on indoor positioning and indoor navigation, Sydney, Australia*, volume 1315, 2012.

[35] Huthaifa Obeidat, Wafa Shuaieb, Omar Obeidat, and Raed Abd-Alhameed. A review of indoor localization techniques and wireless technologies. *Wireless Personal Communications*, 119:289–327, 2021.

[36] Maja Pušnik, Mitja Galun, and Boštjan Šumak. Improved bluetooth low energy sensor detection for indoor localization services. *Sensors*, 20(8):2336, 2020.

[37] Robert Riesebos, Viktoriya Degeler, and Andrés Tello. Smartphone-based real-time indoor positioning using ble beacons. In *2022 IEEE 18th International Conference on Automation Science and Engineering (CASE)*, pages 1281–1288. IEEE, 2022.

[38] Jirapat Sangthong, Jutamas Thongkam, and Sathapom Promwong. Indoor wireless sensor network localization using rssi based weighting algorithm method. In *2020 6th International Conference on Engineering, Applied Sciences and Technology (ICEAST)*, pages 1–4. IEEE, 2020.

[39] L. van de Beek. Accuracy and precision of wireless ultrawideband localization. October 25 2022.

[40] Qing Wang and Marco Zuniga. Passive visible light networks: Taxonomy and opportunities. In *Proceedings of the workshop on light up the IoT*, pages 42–47, 2020.

[41] Tianyu Wang, Hanying Zhao, and Yuan Shen. An efficient single-anchor localization method using ultra-wide bandwidth systems. *Applied Sciences*, 10(1):57, 2019.

[42] Woxu Wireless Ltd. Uwb localization techniques in comparison. `https://uwb.woxuwireless.com/views/blog/UWB_Localization.html`, 2021. Last accessed: Oct. 30, 2023.

[43] Xudong Wu, Ruofei Shen, Luoyi Fu, Xiaohua Tian, Peng Liu, and Xinbing Wang. ibill: Using ibeacon and inertial sensors for accurate indoor localization in large open areas. *IEEE Access*, 5:14589–14599, 2017.

[44] Bo Yang, Jun Li, Zhanpeng Shao, and Hong Zhang. Robust uwb indoor localization for nlos scenes via learning spatial-temporal features. *IEEE Sensors Journal*, 22(8):7990–8000, 2022.

[45] Runming Yang, Xiaolong Yang, Jiacheng Wang, Mu Zhou, Zengshan Tian, and Lingxia Li. Decimeter level indoor localization using wifi channel state information. *IEEE Sensors Journal*, 22(6):4940–4950, 2021.

[46] Faheem Zafari, Athanasios Gkelias, and Kin K Leung. A survey of indoor localization systems and technologies. *IEEE Communications Surveys & Tutorials*, 21(3):2568–2599, Sept 2019.

[47] Minghui Zhao, Tyler Chang, Aditya Arun, Roshan Ayyalasomayajula, Chi Zhang, and Dinesh Bharadia. Uloc: Low-power, scalable and cm-accurate uwb-tag localization and tracking for indoor applications. *Proceedings of the ACM on Interactive, Mobile, Wearable and Ubiquitous Technologies*, 5(3):1–31, 2021.